# **IMAGES-SCAPE2:**

# A modeling study of size- and chemically resolved aerosol thermodynamics in a global chemical transport model

Marco A. Rodriguez and Donald Dabdub

Department of Mechanical and Aerospace Engineering, University of California, Irvine, California, USA

Received 27 March 2003; revised 16 September 2003; accepted 24 September 2003; published 20 January 2004.

[1] Chemically and size-resolved aerosol mass size distributions are simulated online using the Intermediate Model of Global Evolution of Species (IMAGES). Aerosol-phase thermodynamics is coupled to this chemical transport model using the Simulating Composition of Atmospheric Particles at Equilibrium (SCAPE2) module. Emphasis is placed on the equilibrium concentrations of aerosol ammonium, nitrate, sulfate, and water content subject to the interaction with ions from sea salt and dust. Transport for both aerosol and gas-phase species is solved using a semi-Lagrangian scheme driven by monthly mean climatological variables provided by European Centre for Medium-Range Weather Forecasts (ECMWF) analysis. This study presents estimates of annual average dry mass size distributions at selected stations in North America and Europe. Simulations are performed to observe the major differences between the coupled IMAGES-SCAPE2 model and IMAGES alone for key aerosol species. Nitrate concentrations predicted with IMAGES-SCAPE2 compare better with observations than those calculated with IMAGES alone. Model results show that aerosol size distributions are generally bimodal. This study finds that over polluted continental regions, the presence of sea-salt and dust aerosol potentially increases the formation of sulfate by 20-80%. Nitrate formation is enhanced by 14-60%, whereas ammonium formation is decreased by 20-60%. Nitrate plays an important role to determine the size distributions in many European stations. The presence of water changes the general shape of the size distribution, placing maximum values on larger size ranges. Atmospheric Composition and Structure: Aerosols and particles (0345, 4801); 0368 Atmospheric Composition and Structure: Troposphere—constituent transport and chemistry; 3210 Mathematical Geophysics: Modeling; KEYWORDS: aerosol thermodynamics, global chemical transport model, aerosol size distribution

**Citation:** Rodriguez, M. A., and D. Dabdub (2004), IMAGES-SCAPE2: A modeling study of size- and chemically resolved aerosol thermodynamics in a global chemical transport model, *J. Geophys. Res.*, 109, D02203, doi:10.1029/2003JD003639.

### 1. Introduction

[2] Despite substantial progress made in our understanding of aerosols net effect on Earth's climate and atmospheric chemistry, aerosol loads and their distributions remain uncertain as a result of the many production processes involved. Tropospheric aerosols pose the largest uncertainties in model estimates of climate forcing because of manmade changes in the atmosphere's composition [National Research Council (NRC), 1996]. Further development of chemical transport models that produce accurate global aerosol distributions is necessary to reduce these uncertainties. Field studies and satellite observations are critical to understand aerosol impacts, but they provide a partial look at global aerosol distributions over frequently changing atmospheric conditions. Thus mathematical models are essential for quantitative integration of results and for the understanding of coupled physical and chemical aerosol

- processes in the atmosphere. Several regional and global modeling studies focus on the prediction of mass concentrations for one aerosol species alone. For instance, the distribution of sulfate [Benkovitz et al., 1994; Chin et al., 1996; Franceschini et al., 1991; Langner and Rodhe, 1991; Luecken et al., 1991; Pham et al., 1995], mineral dust [Genthon, 1992; Tegen and Fung, 1995; Zhang and Carmichael, 1999], sea-salt [Gong et al., 1997; Erickson et al., 1999], and carbonaceous aerosols [Liousse et al., 1996; Penner et al., 1996]. Generally, these studies describe total aerosol mass or only a few radii set without additional information about the aerosol size distributions.
- [3] In recent years, scientists examined the impact of incorporating more than one aerosol component in global models [Tegen et al., 1997; Takemura et al., 2000; Collins et al., 2001; Ghan et al., 2001a, 2001b; Rasch et al., 2001; Penner et al., 2002; Chin et al., 2002]. These studies investigate the fate of multicomponent aerosol subject to various processes in particular transport. However, just a few [Adams et al., 1999; Jacobson, 2001; Metzger et al., 2002a, 2002b] include an aerosol module that accounts for

Copyright 2004 by the American Geophysical Union. 0148-0227/04/2003JD003639\$09.00

**D02203** 1 of 27

thermodynamics and mass transfer between aerosol and gas phases. On the other hand, many studies incorporate an aerosol module in urban and regional models. In particular, the Simulating Composition of Atmospheric Particles at Equilibrium 2 (SCAPE2) model [Kim et al., 1993a, 1993b; Kim and Seinfeld, 1995; Meng et al., 1995a, 1995b] is used extensively to explore the effects of size- and chemically resolved aerosol in urban environments [Meng et al., 1998; Dabdub et al., 1999; Nguyen and Dabdub, 2002; Knipping and Dabdub, 2003]. Zhang et al. [2000] evaluated and compared SCAPE2 with other aerosol thermodynamics modules. Also, other researchers [Song and Carmichael, 2001a, 2001b; Galy-Lacaux et al., 2001] used SCAPE2 to investigate the interaction of different inorganic aerosol ions in regional models.

[4] This manuscript presents the results of a modeling study in which, for the first time, SCAPE2 is integrated in a size- and chemically resolved aerosol module coupled with the Intermediate Model of Global Evolution of Species (IMAGES), a fully three-dimensional, global-scale Chemical Transport Model (CTM). The large spatial resolution of the host CTM and the use of monthly averaged climatological data are shortcomings inherent to its original formulation. This effort to couple multicomponent aerosol with a three-dimensional CTM extends throughout the entire troposphere for a 2-year simulation. One of the objectives of this work is to provide insights on the potential advantages of incorporating an aerosol thermodynamics module in a global model. Simulations are performed to observe the major differences between the coupled IMAGES-SCAPE2 model and IMAGES alone for key aerosol species. Available observations are used to compare with model results. Finally, simulated size distributions are compared with aerosol size distributions that are traditionally assumed lognormal.

[5] A thorough description of the aerosol module used and the methodology followed to couple the module into the host chemical transport model is detailed in section 2. Section 3 shows results of the modeled global aerosol concentrations. Simulated concentrations are then compared to observations over industrialized regions using available databases. Section 3 concludes with further investigation of the effects on the dynamics of chemically resolved and size-resolved aerosol mass distributions.

### 2. Model Description

### 2.1. Aerosol Module

[6] The size distribution and chemical composition of atmospheric aerosol particles are determined by a complex interaction of physico-chemical processes that include nucleation, condensation, coagulation, and in-cloud processing. There are many approaches to incorporate aerosol dynamics in urban and regional-scale models [Binkowski and Shankar, 1995; Jacobson, 1997]. The present study is based on the methodology previously adopted by Wexler et al. [1994], Lurmann et al. [1997], and Meng et al. [1998]. This approach uses a sectional approximation to represent the aerosol size distribution. Thus the size domain is separated in a series of sections (bins), each with uniform composition. Although ambient particles are not internally mixed with respect to their hygroscopic

properties [Covert and Heintzenberg, 1984; McMurry and Stolzenburg, 1989], limitations in both measurement instrumentation and our understanding of the degree of mixing in aerosol particles, pose serious uncertainties to represent accurately the aerosol mixing state in computational models.

[7] The composition and size evolution of an internally mixed aerosol is described by the general dynamic equation [Wexler et al., 1994]

$$\frac{\partial}{\partial t} q_i(m, \mathbf{x}, t) = -\left(\mathbf{u} - V_s(m)\mathbf{k}\right) \cdot \nabla q_i + \nabla \cdot \left(\mathbf{K}(\mathbf{x}, t) \nabla q_i\right) 
+ H_i(m, \mathbf{x}, t) q(m, \mathbf{x}, t) - \frac{\partial}{\partial m} (q_i H) 
+ \int_0^m \Gamma(m', m - m', \mathbf{x}, t) q_i(m', \mathbf{x}, t) 
\cdot \frac{q(m - m', \mathbf{x}, t)}{m - m'} dm' 
- q_i \int_0^\infty \Gamma(m', m, \mathbf{x}, t) \frac{q(m', \mathbf{x}, t)}{m'} dm' 
+ S_i(m, \mathbf{x}, t) - L_i(m, \mathbf{x}, t) q_i + N_i(m, \mathbf{x}, t) \tag{1}$$

where  $q(m, \mathbf{x}, t)$  is the total mass distribution at a given time t, and point in space  $\mathbf{x} = (x, y, z)$ , such that  $q_i(m, \mathbf{x}, t)dm$  is the mass concentration of species i in the mass range [m, m+dm] and  $\sum_i q_i = q$ ;  $m_i$  is the mass of species i in a particle of total mass m;  $H_i$  is the inverse of the characteristic time for particle growth from condensation or evaporation of species i

$$H_i(m, \mathbf{x}, t) = \frac{1}{m} \frac{dm_i}{dt}; \tag{2}$$

the total normalized growth rate of a particle of mass m is

$$H(m, \mathbf{x}, t) = \frac{1}{m} \frac{dm}{dt} = \sum_{i} H_i(m, \mathbf{x}, t);$$
(3)

 $\Gamma(m',m) = \Gamma(m,m')$  is the binary coagulation coefficient;  ${\bf k}$  is the unit vector in the vertical direction;  ${\bf u}$  is the wind velocity vector;  $V_s$  is the particle gravitational settling velocity;  ${\bf K}$  is the eddy diffusivity tensor;  $S_i$  is the emission rate;  $L_i$  is the first-order rate of removal of species i (wet and dry deposition), and  $N_i$  is the nucleation rate of species i. The transport operator is identical for gas-phase and aerosol-phase species. Therefore the same spatial transport operator is used for the solution of the corresponding terms in equation (1). For computational purposes the variable m is transformed to a normalized particle diameter  $\mu = \ln(D_p/D_{p0})$  where  $D_p$  is the particle diameter and  $D_{p0}$  is a reference diameter.

[8] Wexler et al. [1994] showed that even under the most extreme particle concentrations of urban areas, Brownian coagulation has a negligible effect on the evolution of the aerosol size distribution over considered timescales. Thus coagulation has been neglected in urban [Meng et al., 1998] and regional [Song and Carmichael, 2001a; Dentener et al., 1996] applications. Coagulation is not a process considered in the present study because the spatial resolution of the

global model ensures that aerosol concentrations are sufficiently small compared to those of urban areas.

### 2.1.1. Condensation and Evaporation

[9] The condensation-evaporation rate of species i is given by [Wexler et al., 1994]

$$H_i = \frac{1}{m} \frac{dm_i}{dt} = \frac{2\pi D_p D_i}{m} \frac{C_{\infty,i} - C_{s,i}}{\frac{2\lambda}{\alpha_i D_p} + 1}$$
(4)

where  $D_i$  is the molecular diffusivity of species i in air;  $C_{\infty,i}$  and  $C_{s,i}$  are the concentrations in the bulk gas phase and the particle surface respectively;  $\lambda$  is the air mean free path; and  $\alpha_i$  is the accommodation coefficient for species i on the atmospheric aerosol. Particle surface vapor concentrations  $C_{s,i}$  are estimated by the thermodynamic module described subsequently.

#### 2.1.2. Nucleation

[10] The formation of new particles from a continuous phase is referred to as nucleation. Homogeneous nucleation is assumed to occur only with  $H_2SO_4/H_2O$ . Wexler et al. [1994] used a parameterization in which a nucleation threshold concentration,  $C_{crit}$  (in  $\mu g/m^3$ ) for  $H_2SO_4$  is calculated as

$$C_{crit} = 0.16 \exp(0.1T - 3.5\text{RH} - 27.7)$$
 (5)

where T is the temperature in Kelvin and RH the relative humidity between 0 and 1. If ambient  $H_2SO_4$  vapor concentrations exceed  $C_{crit}$ , the amount of mass exceeding that threshold is removed from the gas phase and placed into the smallest aerosol size section.

## 2.1.3. Aerosol Thermodynamics

[11] The major purpose of the thermodynamical module is the computation of  $C_{s,i}$ . The difference between  $C_{s,i}$  and the bulk gas  $C_{\infty,i}$  is the driving force for the gas-to-particle mass transfer. This study uses SCAPE2 as the thermodynamical module that computes the particle surface vapor concentration. SCAPE2 includes the following ions: sodium, sulfate, ammonium, nitrate, chloride, potassium, calcium, magnesium and carbonates. In addition, the aerosol module contains a comprehensive treatment of inorganic gas-aerosol equilibrium and provides a choice of three algorithms to estimate activity coefficients [Bromley, 1973; Kusik and Meissner, 1978; Pitzer and Kim, 1974]. Activity coefficients in this study are calculated following Kusik and Meissner [1978]. The module also considers the temperature dependence of the deliquescence point.

# 2.2. Aerosol-CTM Integration

[12] The host CTM used is the Intermediate Model of Global Evolution of Species (IMAGES) [Müller and Brasseur, 1995]. This three-dimensional chemical transport model of the troposphere follows the distribution of 53 gas-phase compounds and 125 chemical reactions, including 26 photodissociations. The chemical mechanism is based on the recommendations of De More et al. [1992] and Atkinson et al. [1989] for inorganic chemistry and the NCAR master mechanism [Calvert and Madronich, 1987; Madronich and Calvert, 1989, 1990] for organic chemistry. The simulated tropospheric sulfur cycle is based mostly in previous work by Pham et al. [1995]. The present study

relies primarily on the chemical mechanism and emissions inventory of Pham et al. However, a new treatment of sulfate formation, detailed in the following sections, is implemented with the coupling of the new aerosol module. Horizontal resolution is set at  $5^{\circ}$  latitude by  $5^{\circ}$  longitude, while  $25 \, \sigma$  layers bound the vertical resolution. Sigma is defined [*Phillips*, 1957] as

$$\sigma = \frac{p - p_t}{p_s - p_t} \tag{6}$$

where p is pressure,  $p_s$  is the pressure at the surface, and  $p_t$ is set at 50 mbar. The levels are not equally spaced. Namely, the vertical resolution is highest near the surface to improve the description of vertical exchanges of chemical species within the boundary layer. The approximate thickness of the lowest layer is 40 m (995 mbar), whereas the upper layer is located at approximately 22.5 km from the surface. The computational domain is limited between 85°N and 85°S, which makes the model unsuitable for certain applications such as comparisons with Arctic haze. IMAGES is chosen as the host CTM, in part, to ease the computational costs associated with the calculations of aerosol thermodynamics. In contrast to other CTMs such as GOCART or GISS, IMAGES uses mean monthly meteorological data. IMAGES can be considered intermediate between models in which transport is driven by the dynamics provided at each time step by a general circulation model, and models in which transport is highly parameterized [Müller and Brasseur, 1995]. Therefore IMAGES is expected to reproduce concentrations more suitable for comparison with climatological averages. Integration of the aerosol module into the pre-existing CTM requires further modifications to include those terms unique to the modeled aerosol processes. IMAGES already includes gas-phase precursors such as nitric acid, ammonia and sulfuric acid, necessary for the aerosol module.

[13] Sulfur bearing gases in the atmosphere end with oxidation state S(VI) as this is the thermodynamically stable form of sulfur in the presence of oxygen. Among the main sulfur bearing gases included in this model are sulfur dioxide  $(SO_2)$ , dimethylsulfide  $(CH_3SCH_3)$ , hydrogen sulfide  $(H_2S)$  and carbon disulfide  $(CS_2)$ . Reaction of OH with  $H_2S$ ,  $CS_2$  and dimethylsulfide results in the formation of sulfur dioxide. Further oxidation of  $SO_2$  with OH results in the production of gaseous sulfuric acid  $H_2SO_4(g)$ . Sulfuric acid is one of the input gases (in addition to ammonia and nitric acid) required by SCAPE2 to estimate the amount of inorganic mass that partitions into the aerosol phase. Aqueous-phase chemistry involving  $SO_2$  is described in a subsequent section.

[14] Ammonium and nitrate are important constituents of the atmospheric aerosol. Ammonia (NH<sub>3</sub>) is the gas precursor of the ammonium ion (NH<sub>4</sub>). Ammonia sources are generally associated with animal waste, decomposition of organic material, agricultural activities (fertilizers), and industrial emissions. Nitrate is formed mainly from the reaction of ammonia and nitric acid to form ammonium nitrate or from the dissociation of nitric acid upon dissolution in water. Nitric acid is an oxidation product of NO<sub>x</sub>. Major sources of NO<sub>x</sub> are associated with fossil-fuel com-

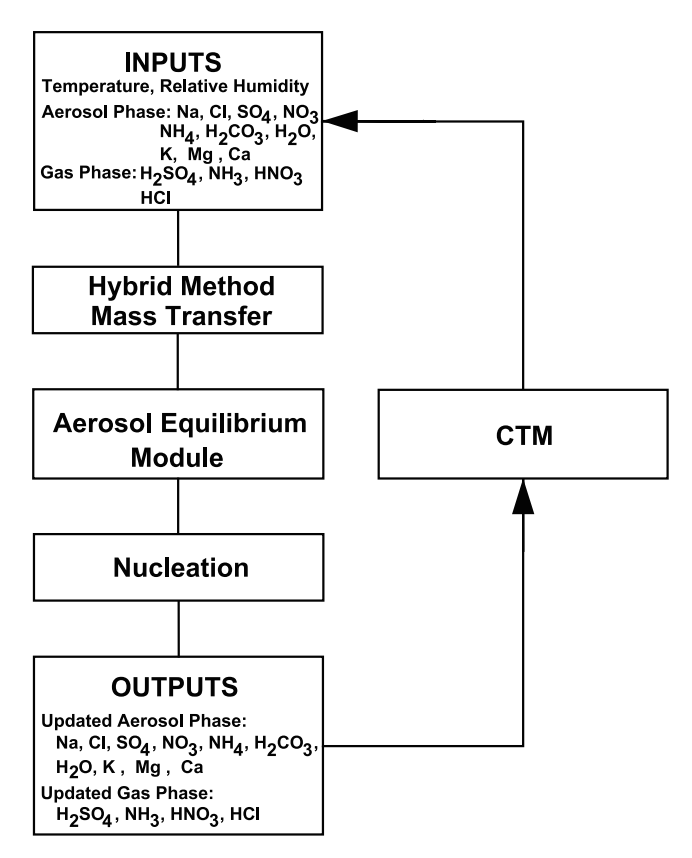


**Figure 1.** Schematic diagram of the main components of the aerosol module and their integration with the global chemistry transport model.

bustion, soil release, (natural and anthropogenic) biomass burning and lightning. Only recently, researchers [Adams et al., 1999, 2001] have included aerosol thermodynamics to account accurately for aerosol nitrate and ammonium in global models. These aerosol types are generally absent from estimates of global radiative effects, in part because of an earlier focus on other principal constituents. For the ammonia-nitric acid-sulfuric acid system, the complete set of possible reactions comprised in the thermodynamic module (SCAPE2) is described by Kim et al. [1993a, 1993b], Kim and Seinfeld [1995], and Meng et al. [1995a, 1995b]. For this system, some useful observations can be determined a priori. When possible, each mole of sulfate removes two moles of ammonia from the gas phase, also the amount of sulfuric acid in the gas phase is negligible. On the basis of these observations, two regimes of interest are defined, the ammonia-rich and the ammonia-poor cases. In the ammonia-poor case, there is insufficient NH<sub>3</sub> to neutralize available sulfate. Thus the aerosol phase is acidic and sulfate tends to drive nitrate to the gas phase. The preferred form of sulfate is bisulfate. In contrast, the ammonia-rich case exhibits excess ammonia and the aerosol is neutralized to a large extent. Ammonia that does not react with sulfate is available to form ammonium nitrate. Competition between sulfate and nitrate for available ammonia results in a rather complex system. For instance, a decrease of sulfate is accompanied by an increase of the aerosol nitrate, but a reduction of aerosol ammonium and total mass. The inclusion of these species in the present model

should lead to more realistic estimates of aerosol distributions than those resulting from assumptions on uniform composition alone.

- [15] IMAGES is modified to accommodate the new aerosol species in all size ranges. The aerosol size domain is discretized in 8 sections, ranging from 0.039 µm to 10 µm. All sections correspond to the equidistant spacing of points along the logarithmic scale of the size domain. Previous studies assumed that certain species follow a lognormal distribution [Tegen et al., 1997; Takemura et al., 2000]. In this study, no a priori assumptions are made regarding the shape of the aerosol size distribution.
- [16] Species whose lifetime is larger than several hours undergo transport by winds, diffusion and cloud convection. The advected gaseous species satisfy the mass conservation equation:

$$\frac{\partial c_i}{\partial t} = -\mathbf{u} \cdot \nabla c_i - \nabla \cdot (\mathbf{K} \cdot \nabla c_i) + P_i - L_i \tag{7}$$

where  $c_i$  are the elements of the gas-phase species concentration vector  $\mathbf{c}$ ; t is time;  $\mathbf{u} = (u, v, w)$  is the advective flow field; **K** is the eddy diffusivity tensor;  $P_i$  and  $L_i$  are the production (e.g., chemistry, emissions) and destruction (chemistry, dry and wet deposition) terms respectively. IMAGES solves equation (7) with a timesplitting numerical technique [McRae et al., 1982]. The model time step for all processes is 6 hours, except during the first 3 days of each month, when a full diurnal calculation is performed with a time step of 1 hour (half an hour during day 3). In the original formulation of IMAGES, Muller et al. recognized that it was expensive in terms of computer time requirements to account for the diurnal cycle throughout the entire simulation. Therefore, in IMAGES, the diurnal cycle is calculated explicitly only during 3 days at the beginning of each month. Diurnally averaged concentrations are calculated during the remaining of the month, using diurnally averaged photodissociation coefficients and reaction rates corrected to account for night/day variations [Müller and Brasseur, 1995]. Advection is addressed using a semi-Lagrangian scheme based on the approach of Smolarkiewicz and Rasch [1991]. The transport scheme is driven by monthly mean climatological variables from the European Centre for Medium-Range Weather Forecasts (ECMWF) analysis. After transport and chemistry are solved, the aerosol operator performs nucleation and condensation-evaporation calculations. These aerosol calculations depend on temperature, relative humidity and the precursor gas-phase concentrations. Averaged meteorological fields are obtained from the ECMWF analysis at every point of the grid and updated every month; whereas gasphase species (nitric acid, ammonia and sulfuric acid) are provided to the aerosol module after the chemistry operator modifies them. The aerosol module then computes the mass transfer between the gas and aerosol phases under thermodynamical equilibrium considerations for all inorganics and establishes the aerosol mass concentration for each bin. Figure 1 shows a schematic of the modules involved in the aerosols coupling into the chemistry transport model.

[17] The conditions under which atmospheric volatile compounds in the gas phase, such as ammonia and nitric acid, approach the equilibrium state with a population of

aerosol particles have been investigated thoroughly [Wexler and Seinfeld, 1990, 1992]. In particular, Meng and Seinfeld [1996] performed systematic studies on the timescales needed to achieve gas-aerosol equilibrium in a box model. These researchers found that at fixed total aerosol mass, equilibration times increase with increasing particle size. Characteristic times for gas-aerosol equilibrium fall within a range of 1 to 4 hours. Since the model time step (6 hours) is larger than these typical timescales, it is reasonable to assume that aerosols achieve thermodynamic equilibrium with the gas phase during one time step. It is not expected from this model to reproduce the short time variations of aerosol concentrations observed in the atmosphere, but values should compare with climatological averages. The aerosol/gas mass transfer in the model uses a hybrid method described by Pandis et al. [1993] and Lurmann et al. [1997].

[18] The coupled model is integrated for a period of two simulation years. A typical simulation requires a 12-month spin-up time to generate background values used as initial concentrations for the production run during the successive 12 months. Meteorological data for the production run is the same as that used during the initialization period. Any particular initial values are not relevant for the final output, since this study only considers aerosol concentration trends under characteristic atmospheric conditions, over long periods of time. The model results are intended to represent the atmosphere during a typical year of the 1980 decade, following the original formulation of IMAGES. Model results are not sensitive to initial conditions after the 12-month initialization period. This model requires 7 days of CPU time on a single Athlon XP 2100+ processor ( $\sim$ 1.7 GHz) to complete one 2-year simulation.

# 2.2.1. Dry Deposition

[19] Dry deposition is included as a ground level boundary condition in terms of an empirical parameter (deposition velocity) for all species [Russell et al., 1993]. Aerosol dry deposition uses a resistance-in series parameterization of Wesely and Hicks [1977]. The deposition velocity,  $v_d$ , for particles is based on

$$v_d = \frac{1}{r_a + r_b + r_a r_b v_s} + v_s \tag{8}$$

where  $r_a$  and  $r_b$  are the aerodynamic and quasi-laminar resistances respectively. The gravitational settling velocity  $v_s$  is given by Stokes law. Our estimate of particle settling velocity does not account for differences in density due to chemical speciation. Typical values for the deposition velocity vary from 0.01 to 1 cm/s, depending on particle size.

#### 2.2.2. Wet Removal

[20] Washout parameterization is based on the satellite distribution of optically thick clouds from the International Satellite Cloud Climatology Project (ISCCP) [Rossow et al., 1987; Rossow and Schiffer, 1991] and the climatological precipitation rates from the climatology of Shea [1986]. The coverage distribution of Nimbostratus (Ns) and Cumulonimbus (Cb) is assumed to be proportional to the middle (pressure top between 680 and 440 mbar) and upper (pressure top higher than 440 mbar) thick clouds from ISCCP. The proportionality coefficients in these relation-

ships are derived from constraints represented by the observed storm parameters (average storm duration and average duration of dry periods) reported by *Thorp* [1986] for the northeastern United States. In this study Cb refers not only to convective cells, but also to the precipitation fraction of stratiform detrainment clouds (the anvil) associated with the Cb. Both, the convective cells and the associated anvils are part of the Mesoscale Convective Systems (MCS) that are described extensively elsewhere [Houze, 1993; Fritsch et al., 1986]. In IMAGES, stratiform precipitation is assumed to account for no more than 40% of the total precipitation associated with MCS. The fraction of the total precipitation rate contributed by Ns and Cb is estimated from their respective fractional areas assuming that the Cb to Ns precipitation rates ratio is equal to  $15 \times p_e$ , where  $p_e$  is the convective precipitation efficiency. This efficiency is defined as the ratio of precipitation to total water vapor inflow in the convective cell.  $p_e$  is calculated as a function of the vertical wind shear following Fritsch and Chappel [1980]. The fractional areas covered by convective cells and anvils are then estimated by requiring a precipitation intensity threshold of at least 10 mm h<sup>-1</sup> in the convective cell [Berkowitz et al., 1989]. Duration of a typical storm is obtained from Feigelson [1984].

[21] Scavenging of soluble gases and aerosols in the updrafts of the convective cells is included in the convection parameterization, as described by Müller and Brasseur [1999]. For highly soluble gases and cloud condensation nuclei (CCN), a fraction equal to the precipitation efficiency (the ratio of precipitation to total water vapor inflow, parameterized as a function of the vertical wind shear) is washed out during the convective updraft. Rainout/washout by stratiform clouds (either Ns or anvils) is represented as a first-order loss process. The sporadic nature of precipitation is accounted by following the parameterization proposed by Rodhe and Grandell [1972], which predicts residence times in good agreement with the results of a time-dependent numerical model using randomly distributed precipitation events [Stewart et al., 1990]. Residence times calculated by these authors assuming random rain agree with observed aerosol lifetimes in the northeastern United States.

[22] The first-order loss rate is a function of the scavenging rate during the precipitation event, the mean precipitation period, and the mean wet and dry ratios. In our climatological model, the mean wet ratio corresponds to the rain cloud coverage. Inside the cloud, the scavenging rate for very soluble gases and aerosols is equal to the rate of conversion of cloud droplets into rain droplets, which is in the order of  $0.001 \text{ s}^{-1}$  [Curry et al., 1990]. For less soluble gases, this rate is multiplied by the liquid-phase fraction, dependent on solubility and liquid water content. For fairly soluble compounds, the precise value of the scavenging rate is unimportant. Below-cloud scavenging rates for aerosols are parameterized as a function of precipitation intensity, on the basis of literature data [Dai, 2001; Mishra and Sharma, 2001; Barrett, 1970]. This parameterization will require further work to account for the rate's dependence on particle size and composition, as well as the different hygroscopic characteristics of each aerosol type.

[23] An extensive validation of the wet deposition scheme using <sup>210</sup>Pb concentrations is beyond the scope of this work. *Giannakopoulos et al.* [1999] offered a

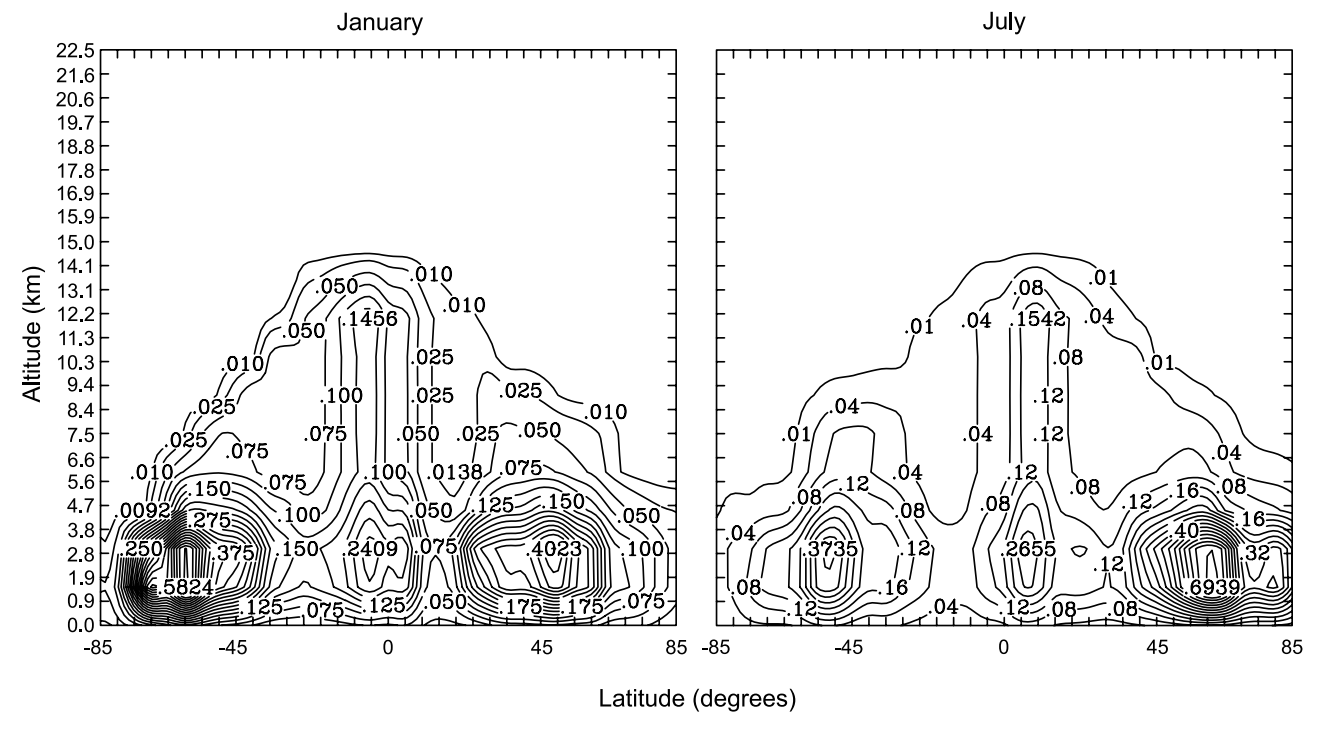


Figure 2. Zonal mean scavenging frequency (d<sup>-1</sup>) of Pb for January and July.

complete inter-comparison of wet and dry deposition schemes in the TOMCAT off-line chemical transport model. These researchers concluded that aerosol residence times are realistic only when wet removal schemes use precipitation rates rather than specific humidities. IMAGES uses various satellite and literature parameters to model these precipitation rates. Figure 2 shows the zonal mean scavenging frequency of Pb in d<sup>-1</sup> for January and July as obtained from IMAGES. These figures are similar to those reported by Giannakopoulos et al.

# 2.2.3. Aqueous-Phase Chemistry

[24] Dissolution of  $SO_2$  in water results in the formation of  $HSO_3^-$  and  $SO_3^{2-}$ . At pH values less than  $\sim 5$  the predominant oxidation pathway for sulfate formation is by  $H_2O_2$  oxidation. Whereas at pH > 5, oxidation with  $O_3$  starts to be the dominant pathway. In-cloud  $SO_2$  oxidation in this study is a modified formulation from the original implementation, based on *Pham et al.* [1995]. The new formulation reflects oxidant limitation dependence on hydrogen peroxide and ozone concentrations. Expressions for the rate of reaction of S(IV) with dissolved ozone and hydrogen peroxide are [Hoffmann and Calvert, 1985]

$$\left| \frac{d[S(IV)]}{dt} \right| = \left( k_0[SO_2H_2O] + k_1[HSO_3^-] + k_2[SO_3^{2-}] \right) [O_3] \quad (9)$$

and

$$\left| \frac{d[S(IV)]}{dt} \right| = \frac{k_3[H^+]}{1 + 13[H^+]} [HSO_3^-] [H_2O_2]$$
 (10)

respectively. Thermodynamic and kinetic data used are summarized in Tables 1 and 2. These rates are applied in cells where there are nonprecipitating clouds as determined with ISCCP data. For each cloud type, liquid water content values are obtained from *Heymsfield* [1993]. Bin allocation for sulfate inside the clouds is calculated with the aerosol module previously described.

[25] The inclusion of heterogeneous reactions such as

$$HNO_3(g) + NaCl(aerosol) \rightleftharpoons HCl(g) + NaNO_3(aerosol)$$

are considered in the model through the thermodynamic module SCAPE2 [Kim et al., 1993a, 1993b, Kim and Seinfeld, 1995; Meng et al., 1995a, 1995b], where the full set of multiphase equilibrium (gas-liquid-solid) reactions are detailed. Heterogeneous reactions on dust and sea-salt particles are considered to the extent that the cations present in the aerosol facilitate the condensation of acid gases. However, surface reactions are not included.

Table 1. Chemical Reactions and Rate Constants for Sulfur Aqueous Chemistry

Reaction <sup>a</sup>	$k_{298}$ , $^{\rm b}$ ${\rm M}^{-1}{\rm s}^{-1}$	-E/R, K	Reference
$S(IV) + O_3(aq) \rightarrow S(VI) + O_2$	$k_0 = 2.4 \times 10^4$		Hoffmann and Calvert [1985]
	$k_1 = 3.7 \times 10^5$	-5530	
	$k_2 = 1.5 \times 10^9$	-5280	
$S(IV) + H_2O_2(aq) \rightarrow S(VI) + H_2O$	$k_3 = 7.5 \times 10^7$	-4430	McArdle and Hoffmann [1983]

<sup>&</sup>lt;sup>a</sup>Reaction with "nonelementary" rate expression. See section 2.

<sup>&</sup>lt;sup>b</sup>The temperature dependence is represented by  $k = k_{298} \exp[(-E/R)(1/T - 1/298)]$ , where k is the reaction rate constant at temperature T (in K).

**Table 2.** Equilibrium Reactions

Reaction	$K_{298}^{\text{a}} \text{ M or M atm}^{-1}$	$-\Delta H/R$ , K	Reference
$SO_2 \cdot H_2O  HSO_3^- + H^+$	$1.3 \times 10^{-2}$	1960	Smith and Martell [1976]
$HSO_3^- SO_3^{2-} + H^+$	$6.6 \times 10^{-8}$	1500	Smith and Martell [1976]
$SO_2(g)$ $SO_2(aq)$	1.23	3120	Pandis and Seinfeld [1989]
$O_3(g)$ $O_3(aq)$	$1.13 \times 10^{-2}$	2536	Pandis and Seinfeld [1989]
$H_2O_2(g)$ $H_2O_2(aq)$	$7.45 \times 10^4$	7302	Pandis and Seinfeld [1989]

<sup>a</sup>The temperature dependence is represented by  $K = K_{298} \exp[(-\Delta H/R)(1/T - 1/298)]$ , where K is the reaction rate constant at temperature T (in K).

# 2.2.4. Aerosol Emissions

#### 2.2.4.1. Mineral Dust

[26] Atmospheric mineral dust is found throughout the entire globe, largely because of long-range transport over thousands of kilometers driven by the general circulation of the atmosphere. The importance of dust is evident as potential source areas cover about a third of the Earth's land surface [Meigs, 1953]. Monthly mean dust emissions for the last four sectional bins (0.625 to 10 μm) are provided by the climatology estimated with the mineral Dust Entrainment And Deposition (DEAD) model [C. S. Zender, University of California Irvine, personal communication, 2002; Zender et al., 2003]. Soil and crustal material are composed mainly of Si, Al and Fe [Seinfeld and Pandis, 1998]. Table 3 shows the assumed dust composition. This composition is fixed for all dust types [Pye, 1987; Wang, 1999]; however, this could be an important source of uncertainty for mineral cation concentrations [Song and Carmichael, 2001a]. The present study does not include any aerosol emissions from biomass or biofuel sources.

# 2.2.4.2. Sea Salt

[27] The most prominent mechanism responsible for seasalt production over the open ocean is believed to be the entrained air bubbles bursting during whitecap formations because of surface wind [Blanchard and Woodcock, 1980]. Sea-salt particles emissions are based on Monahan et al. [1986] formulation when bubble bursting is the only generation mechanism:

$$\frac{dF}{dr} = 1.373 \ U_{10}^{3.41} \times 10^{1.19e^{-B^2}} \frac{1 + 0.057r^{1.05}}{r^3}$$
 (11)

where  $B = (0.380 - \log r)/0.650$ .  $U_{10}$  is the wind speed 10 meters above the water surface. This study uses, however, the estimated wind speed at the first sigma level (~40 m). At each point in the surface, this value depends on the zonal, meridional and sigma wind components of the ECMWF data. The density function dF/dr (particles m<sup>-2</sup>

Table 3. Composition of Emitted Dust Particles

Species	Percent by Weight
Al <sub>2</sub> O <sub>3</sub> , SiO <sub>2</sub> <sup>a</sup>	64.81
Al <sub>2</sub> O <sub>3</sub> , SiO <sub>2</sub> <sup>a</sup> Ca <sup>2+</sup>	6.80
$Fe_2O_3^{a}$ $Na^+$ $K^+$ $Mg^{2+}$	4.49
Na <sup>+</sup>	1.60
$K^{+}$	0.91
$Mg^{2+}$	0.78
Others <sup>a</sup>	20.61

<sup>&</sup>lt;sup>a</sup>Inert species considered as other inorganics in SCAPE2.

s<sup>-1</sup> μm<sup>-1</sup>) expresses the rate at which sea-salt droplets are generated per unit area of surface F, and per increment of droplet radius r. Fluxes over each sectional bin are obtained by integration of equation (11). This equation is valid for particles with diameter less than 10 µm, the upper limit considered here. Monthly emission inventories of sea-ice data, obtained from a geographical atlas [Kartographisches Institut Bertelsmann, 1977], mask areas where ice coverage inhibits bubble generated sea-salt production. The chemical composition of freshly emitted sea-salt particles (Table 4) is similar to that of seawater [Seinfeld and Pandis, 1998]. The emitted particles are as alkaline as seawater with pH  $\sim 7.7$ to 8.8 depending on temperature and salinity [Millero, 1986]. Once sea-salt particles are released into the atmosphere, SCAPE2 establishes equilibrium between the aerosol and the ambient gases accounting for relative humidity, temperature, and composition. This approach allows the model to determine the fate of aerosols after being generated in the oceans surface. In order to correct for possible sea-salt flux underestimation due to use of monthly averaged meteorological data, a multiplicative factor is adopted. For each month, sea-salt emission flux in each bin is modified such that the total Cl mass fraction matches the total monthly sea-salt Cl flux estimated by Erickson et al. [1999] climatology.

### 3. Model Results

[28] The following section analyzes the results obtained with the new coupled aerosol-CTM model. First, the most relevant aspects of total aerosol mass concentration are described at the global scale. Comparison between results with the new coupled model (IMAGES-SCAPE2) and results with IMAGES alone are discussed. In addition, evaluation of the coupled model with available data at ground-based stations in North America and Europe is provided to assess model performance. Finally, estimates of modeled aerosol size distributions at selected sites in North America and Europe are presented, and the impacts

Table 4. Composition of Emitted Seawater Particles

Species	Percent by Weight	
Cl <sup>-</sup>	55.04	
Cl <sup>-</sup> Na <sup>+</sup>	30.61	
ss-SO <sub>4</sub> <sup>2</sup> Mg <sup>2+</sup> Ca <sup>2+</sup> K <sup>+</sup>	7.68	
$Mg^{2+}$	3.69	
Ca <sup>2+</sup>	1.16	
$K^{+}$	1.10	
Br <sup>-</sup>	0.19	
Others <sup>a</sup>	0.53	

<sup>&</sup>lt;sup>a</sup>Inert species considered as other inorganics in SCAPE2.

on the size distribution analyzed when water content is explicitly accounted.

#### 3.1. Global Aerosol Concentrations

[29] Annually averaged concentrations at the surface level for major species simulated with the coupled aerosol-CTM are shown in Figure 3. Concentrations presented in this figure represent the combined effect of chemical transformation, in addition to sea-salt and dust emissions. In general, results reproduce certain features such as high sulfate over industrialized regions. This has been previously recognized by other researchers [Benkovitz et al., 1994; Chin et al., 1996]. For instance, over the North American east coast and central Asia, sulfate concentrations reach values of 13 µg SO<sub>4</sub>/m<sup>3</sup> during summer. The east coast of China exhibits the largest sulfate concentrations during late fall and winter seasons ( $\sim 10 \mu g SO_4/m^3$ ). In the Southern Hemisphere, southern Africa exhibits values as high as 10 μg SO<sub>4</sub>/m<sup>3</sup> between April and May. Southern Africa is a major source of aerosols in the Southern Hemisphere. Aeolian dust and industrial sulfate are the major constituents of this aerosol [Piketh et al., 1999]. In remote continental areas, typical concentrations vary between 0.1 and 6 μg SO<sub>4</sub>/m<sup>3</sup>, whereas marine areas report maximum values of 4 μg SO<sub>4</sub>/m<sup>3</sup> in the Northern Hemisphere. The contribution of sea-salt sulfate is particularly noticeable in the Southern Ocean (2 to 4 μg SO<sub>4</sub>/m<sup>3</sup>) where strong winds increase particulate emissions.

[30] To investigate the effect of dust and sea salt in sulfate, nitrate and ammonium aerosol concentrations, two different model simulations are performed. One simulation includes aerosols of sea-salt and dust origin, whereas the other neglects these components. Figure 4a shows the averaged relative difference between these model results, defined as

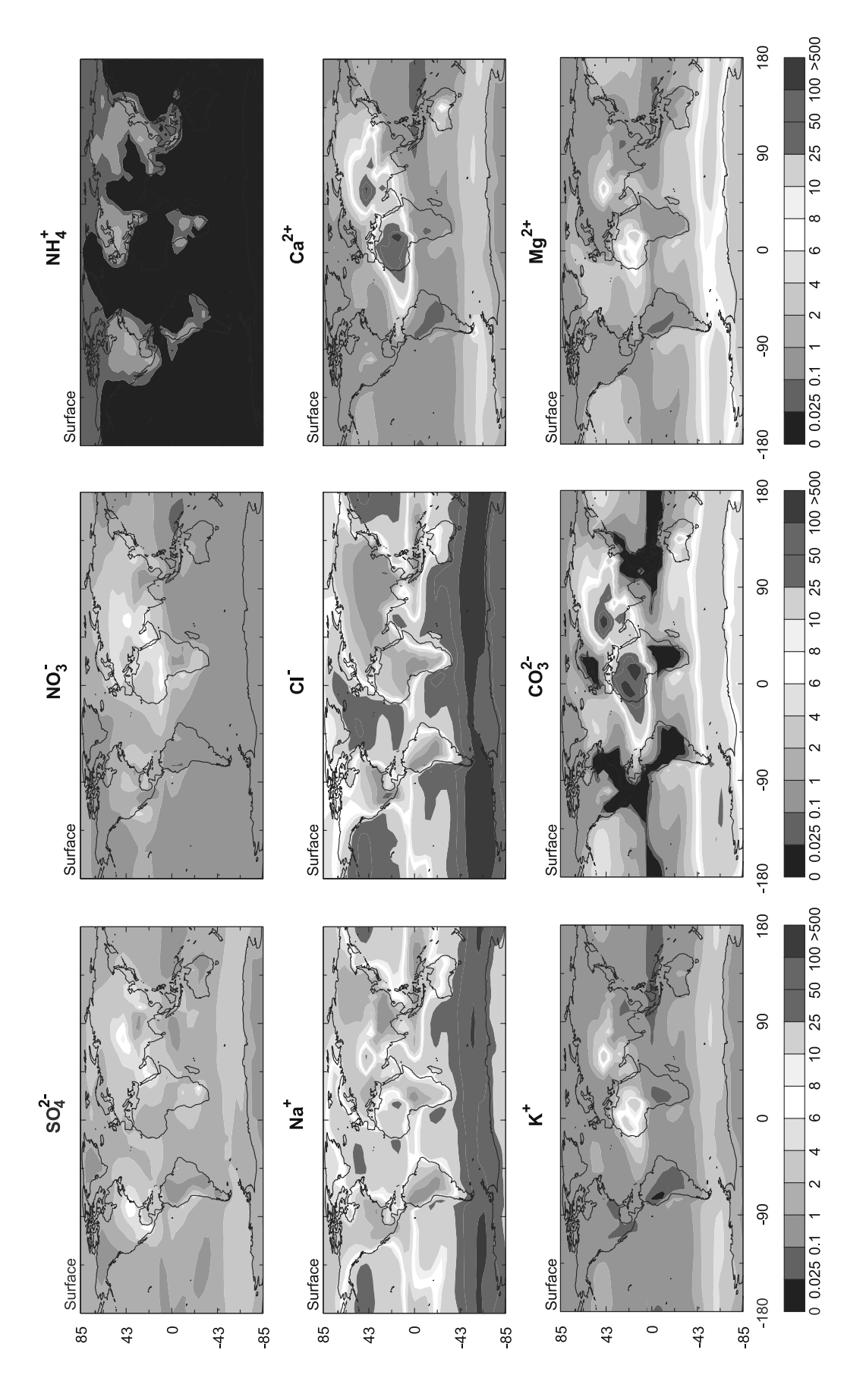
Relative difference in 
$$SO_4^{2-}$$
 % =  $\frac{SO_4^{2-}(ss) - SO_4^{2-}(no - ss)}{SO_4^{2-}(ss)} \times 100$ , (12)

where  $SO_4^{2-}$ (ss) and  $SO_4^{2-}$ (no-ss) are sulfate concentrations with and without sea-salt and dust aerosol respectively. This figure shows that for the most part, sulfate aerosol is enhanced. Over polluted continental regions, the presence of sea-salt and dust aerosol increases the concentration of sulfate by 20-80%. The simulation without sea salt excludes direct sulfate emissions, which explains the increase of 100% or more sulfate in the Southern Ocean and the northeastern Pacific. Figure 5a shows the annually averaged coarse mode (>1.25 µm) to total sulfate ratio at surface level. The observed 100% enhancement in sulfate, resides mostly in the coarse mode, consistent with the composition of sea-salt emissions. Figure 4a also exhibits that sulfate concentrations are reduced by 10% to 20% in the Eurasian Arctic. When alkaline aerosol such as sea salt is included, it attracts acid uptake more favorably. However, Figure 3 shows that the impact of sea salt and dust are relatively small in this region because sea-ice inhibits seasalt production and is not close to dust sources, thus the aerosol tends to attract less sulfate. Fine mode sulfate dominates (>90% of the mass) most of the continental regions as shown in Figure 5a. However, areas like the

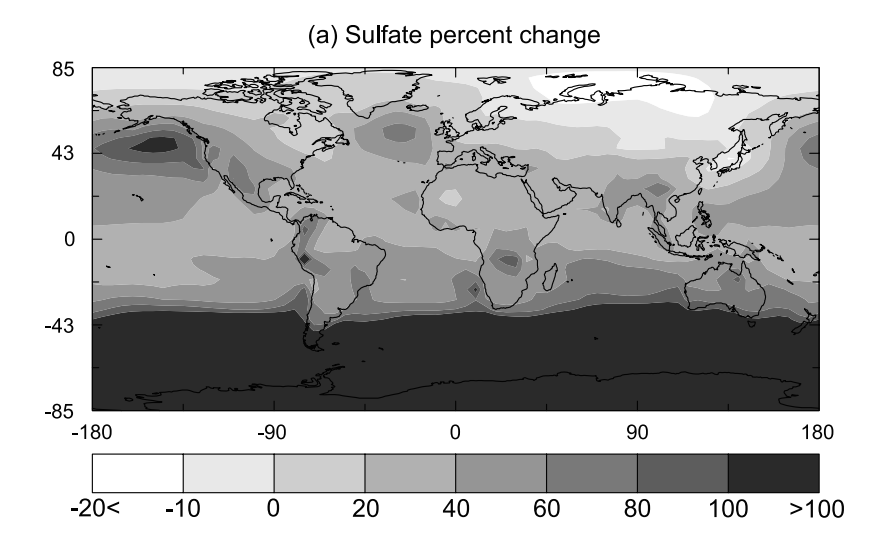
African west coast show that up to 20% of the sulfate resides in the coarse mode. Figure 5a suggests that the observed sulfate enhancement in polluted continental regions occurs in the fine mode. Oxidation of  $SO_2$  to form sulfate favors the formation of a less volatile strong acid that ultimately displaces other acids, such as HCl and HNO3, out of the aerosol. Sulfuric acid then accumulates in the fine mode because it is the first to transfer to the particles with the highest surface to volume ratios (the smallest particles). In addition, the nucleation mechanism also places sulfate in the smallest bin. Once  $H_2SO_4$  is transferred to the particulate phase, then  $HNO_3$  and HCl follow this process. Furthermore, the fact that no surface reactions are included, hinders sulfate formation in the coarse mode.

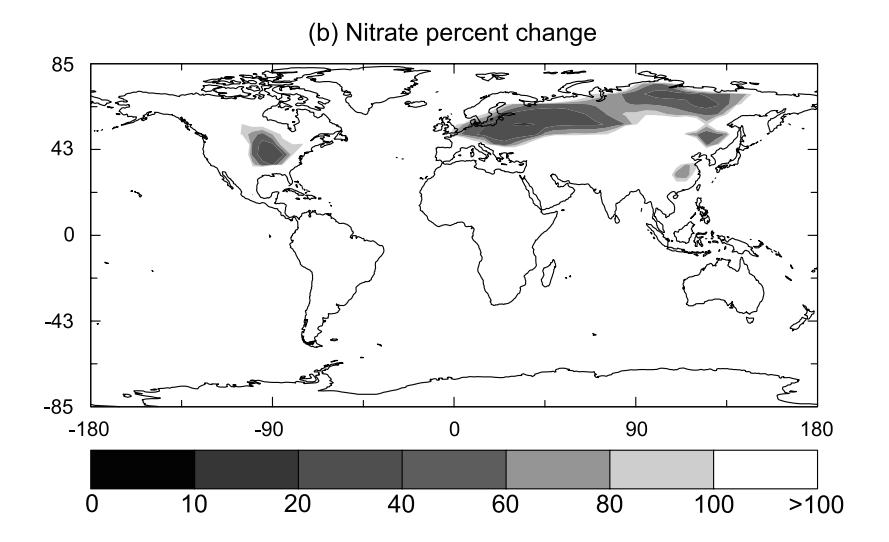
[31] Annually averaged nitrate concentrations are shown in Figure 3. On average, modeled surface nitrate concentrations are slightly higher in Europe than the North American east coast. This is the result of the competition between sulfate and nitrate for available ammonia. A decrease of sulfate in Europe (relative to North America) is accompanied by an increase of the aerosol nitrate. Maximum nitrate concentrations in Europe are reached during the spring, where they are as large as  $10 \mu g \text{ NO}_3/\text{m}^3$ . On the east coast of North America, maxima appear on winter (6-8 μg NO<sub>3</sub>/m<sup>3</sup>), whereas on the west coast nitrate is systematically higher throughout the year, showing a maximum around 8 µg NO<sub>3</sub>/m<sup>3</sup> during summer. Nitrate on the east coast of China peaks during winter months (8 μg NO<sub>3</sub>/m<sup>3</sup>) and decreases to less than 0.025 µg NO<sub>3</sub>/m<sup>3</sup> on the summer, reflecting a similar behavior as nitrate on the North American east coast. The present model results are comparable to previous studies [Adams et al., 1999; Metzger, 2000]. The presence of dust improves aerosol nitrate production [Zhang et al., 1994; Phadnis and Carmichael, 2000; Song and Carmichael, 2001a]. The highest nitrate concentrations at the surface level coincide with regions where dust sources are significant, such as Africa, Saudi Arabia and central Asia. Nitrate in those areas is as high as 25 µg NO<sub>3</sub>/m<sup>3</sup> during the spring season. Also, sea salt enhances nitric acid condensation into the aerosol phase [Nadstazik et al., 2000; Pakkanen, 1996]. In order to measure the effects of sea salt and dust, a relationship similar to equation (12) is defined for nitrate. Figure 4b shows the averaged relative difference between these model results. The increase in nitrate is quite important, as we estimated an enhancement of 14-60% over industrialized regions of the world (Europe and North America). However, the effect is more important over the rest of the domain where the presence of dust, but more importantly sea salt, increases nitrate concentrations more than 100%. Figure 5b shows the estimated coarse mode nitrate to total nitrate ratio at the surface level. Model results show that fine mode nitrate dominates (>80% of the mass) over most regions in the domain.

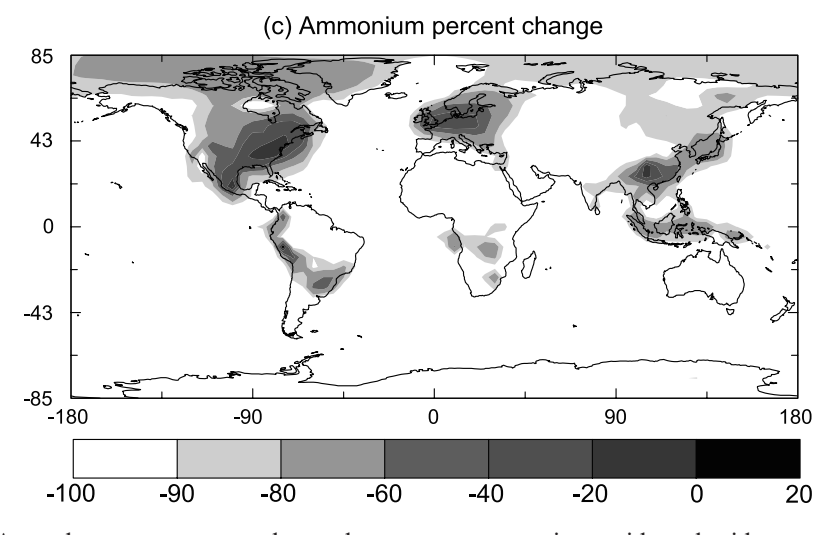
[32] At the surface level, the highest annually averaged ammonium concentrations (Figure 3) are located over industrialized regions where the fate of this aerosol component is closely tied to the relative abundances of nitrate and sulfate. Differences in ammonium concentrations from a simulation run without sea-salt and dust aerosol are compared in Figure 4c. This figure shows that for most regions in the globe, there is a 100% decrease in ammonium



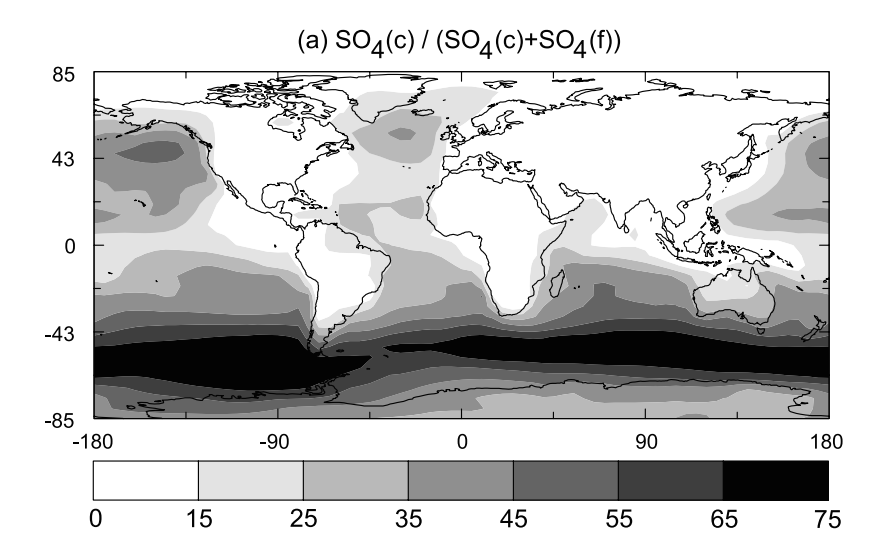
sulfate ( $\mu g SO_4/m^3$ ), nitrate ( $\mu g NO_3/m^3$ ), ammonium ( $\mu g NH_4/m^3$ ), sodium, chloride, calcium, potassium, carbonate and magnesium ( $\mu g/m^3$ ) at surface level. All concentrations include the effect of dust and sea-salt emissions. See color verson of this figure at back of this issue. Global distributions of annual average aerosol mass concentrations calculated with IMAGES-SCAPE2 for Figure 3.

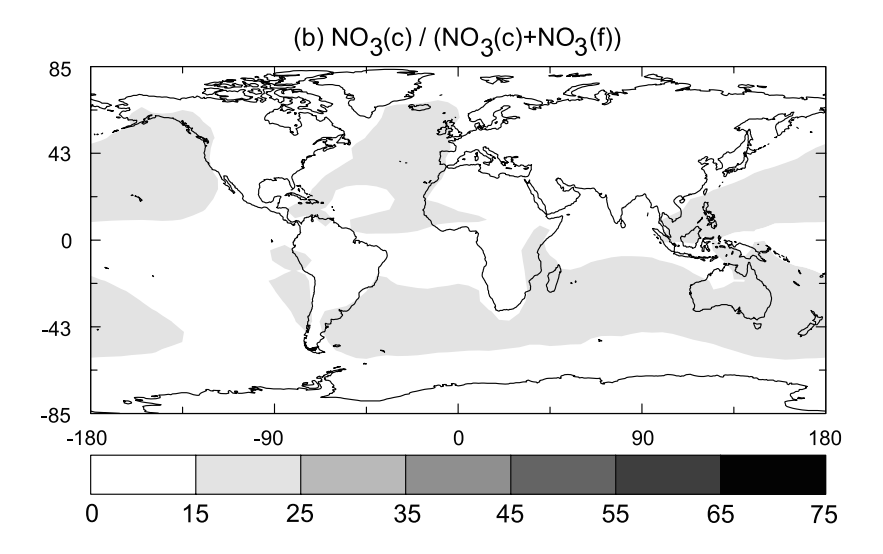






**Figure 4.** Annual average percent change between concentrations with and without sea-salt and dust aerosol contribution for (a) sulfate, (b) nitrate, and (c) ammonium ions.





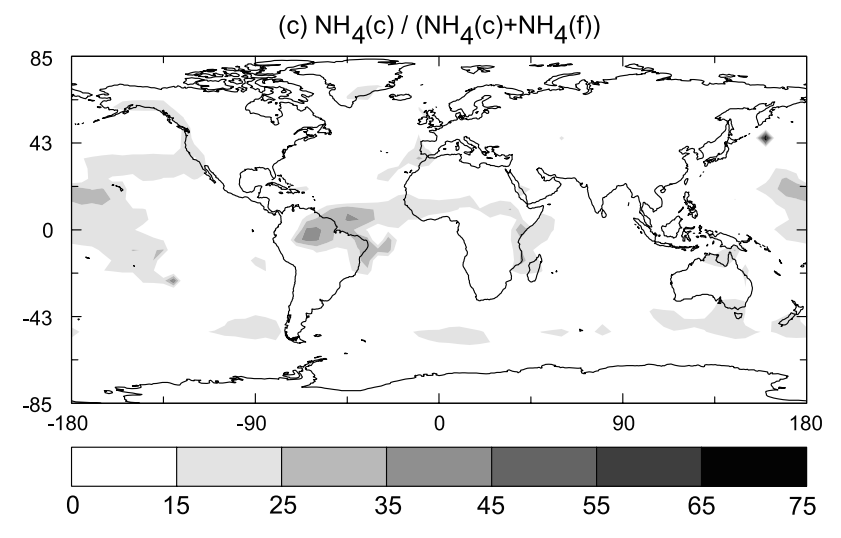


**Figure 5.** Annually averaged ratio of (a) coarse-mode sulfate to total sulfate, (b) coarse-mode nitrate to total nitrate, and (c) coarse-mode ammonium to total ammonium at surface level. This study considers that aerosol with diameters  $>1.25 \mu m$  resides in the coarse mode.

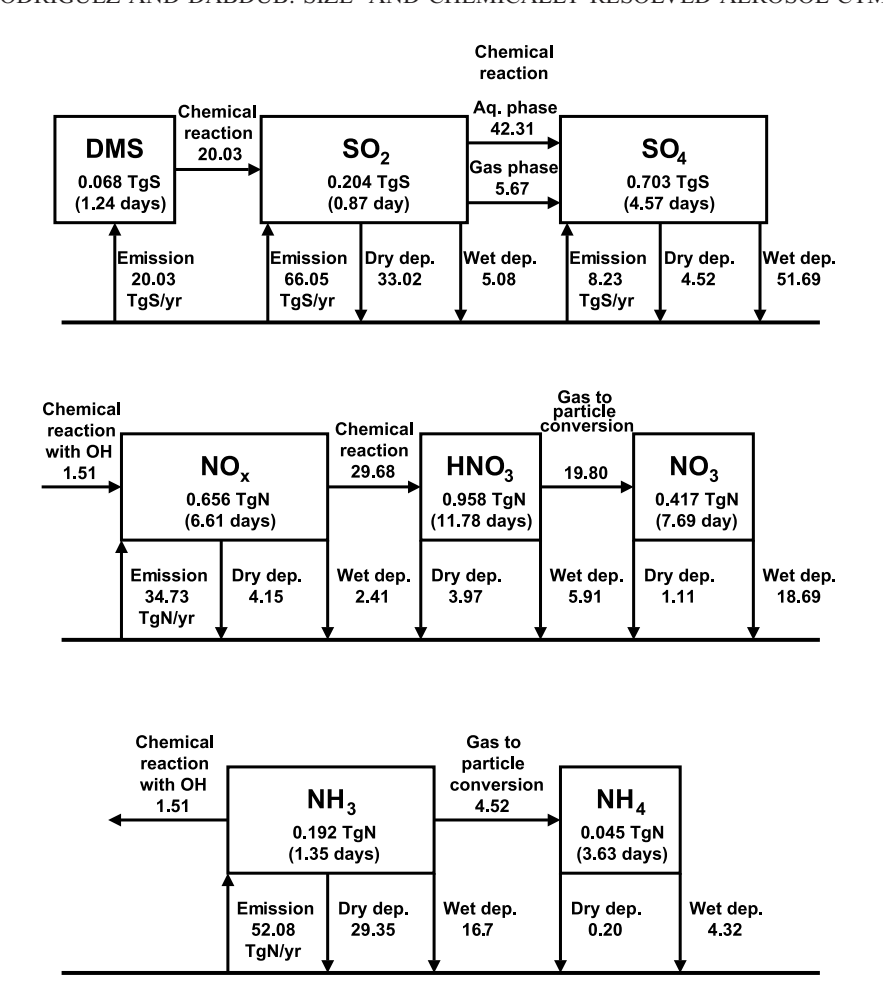


**Figure 6.** Schematic diagram of the global budgets of aerosol species calculated with the IMAGES-SCAPE2 model. Burdens in Tg N (Tg S for the sulfur cycle) and lifetimes are shown inside the boxes. Arrows indicate emissions, deposition fluxes, and conversion into other compounds in Tg N/yr (Tg S/yr for the sulfur cycle). Estimates include the presence of sea salt and dust.

concentrations. However, this loss is less pronounced in continental polluted regions, where this decrement ranges between 20 and 60%. Figure 5 shows that most of the ammonium at the surface level exists in the fine mode. This reduction is partly explained by the presence of cations tied to sea salt and dust. The abundance of this cations makes it difficult for  $NH_3$  to partition into the aerosol phase.

# 3.2. Global Budgets

[33] Global budgets and mass fluxes calculated with the coupled model for relevant aerosol phase species and their gas precursors are summarized on Figure 6. Table 5 presents both values for the sulfur budget: those including the contribution of sea salt and dust (hereinafter referred as ss + d), and estimates in which these aerosol components have been neglected. In addition, Table 5 compares the present work estimates with those from previous studies. It is of particular interest to compare with values calculated by *Pham et al.* [1995], because their study is also based on IMAGES.

[34] The calculated DMS burden is set at 0.06 Tg S (0.068 Tg S with ss + d) Tg S with a lifetime of 1.1 days (1.24 days with ss + d). The inclusion of dust and sea salt

does not change significantly the burden or lifetime of DMS. Furthermore, estimates presented here are similar to other reported values in Table 5. In particular, the DMS budget does not differ considerably from that reported by Pham et al. [1995]. The SO<sub>2</sub> lifetime is found to be 0.87 days with ss + d, which is in the low range but still in the same order of magnitude of values presented by the other studies. Calculated SO<sub>2</sub> burden and lifetime are comparable to those reported by Pham et al. From the different contributions to the global SO<sub>2</sub> sink when sea salt and dust are included, 38.4% is due to dry deposition, 5.9% to wet deposition, 49.2% is the result of aqueous phase oxidation, whereas 6.6% is lost via gas phase oxidation. Pham et al. set these estimates at 45.1% for dry deposition, 4.1% for wet deposition, 45.5% for aqueous phase oxidation and finally 5.3% for gas phase oxidation.

[35] The estimated sulfate lifetime (4.57 days with ss  $\pm$  d) is within the range of values reported in other studies (2.6 to 5.8 days). Wet deposition is the major sink for sulfate. From the total sulfate deposition (56.21 Tg S/yr with ss  $\pm$  d), 92% is due to wet deposition alone. The sulfate burden (0.703 Tg S with ss  $\pm$  d) also falls within the range of previous estimates between 0.63 and 0.8 Tg S. Following *Chin et* 

Table 5. Comparison of Sulfur Budget With Other Studies

Budget	This	COCAPT	CIGGS	Langner and Rodhe	Pham et al.	Feichter et al.	Takemura et al.
Component	Work <sup>a</sup>	GOCART <sup>b</sup>	GISS <sup>c</sup>	[1991]	[1995]	[1996]	[2000]
Burden, Tg S							
$SO_4$	0.545 (0.703)	0.630	0.730	0.77	0.80	0.61	0.456
$SO_2$	0.252 (0.204)	0.430	0.560	0.30	0.20	0.43	0.230
DMS	0.060 (0.068)	0.073	0.056	0.13	0.05	0.10	0.088
Lifetime, days							
$SO_4$	5.2 (4.57)	5.8	5.7	5.3	4.7	4.3	2.6
$SO_2$	1.1 (0.87)	1.8	2.6	1.2	0.6	1.5	1.2
DMS	1.1 (1.24)	2.0	1.9	3.0	0.9	2.2	2.4
Sources, Tg S/yr							
SO <sub>4</sub> production	37.96 (47.98)	38.5	44.7	49.8	62.0	51.3	65.0
SO <sub>2</sub> production	20.03 (20.03)	11.9	10.0	17.0	18.7	16.9	13.3
SO <sub>4</sub> emission	(8.23)						
SO <sub>2</sub> emission	66.05 (66.05)	78.4	70.4	77.5	104.1	83.6	71.8
DMS emission	20.03 (20.03)	13.3	10.7	16.0	20.0	16.9	13.3
Deposition, Tg S/yr							
SO <sub>4</sub> dry deposition	6.54 (4.52)	5.1	9.2	8.6	17.0	6.7	7.7
SO <sub>4</sub> wet deposition	31.42 (51.69)	34.7	37.4	44.5	45.0	44.6	57.3
SO <sub>2</sub> dry deposition	36.34 (33.02)	41.2	35.5	30.5	55.0	40.2	11.7
SO <sub>2</sub> wet deposition	11.78 (5.08)	10.6	0.2	14.2	5.8	9.0	8.4

<sup>&</sup>lt;sup>a</sup>Values in parentheses include the contribution of sea-salt and dust aerosol.

al. [2000a], a sulfate production efficiency is defined as the amount of sulfate produced relative to the total amount of SO<sub>2</sub> emitted and produced in the atmosphere. This reflects the effectiveness of SO<sub>2</sub> oxidation compared to dry and wet deposition processes. The present study finds this effectiveness equals 0.55. This indicates that slightly more than half of the SO<sub>2</sub> contributes to sulfate production in the atmosphere and the rest is deposited to the surface. Chin et al. found that for the GOCART model typical production efficiencies range between 0.41 and 0.42, whereas a similar estimate for *Pham et al.* [1995] gives 0.51.

[36] Nitrate and ammonium budgets summaries, in addition to comparisons with other studies are shown in Table 6. Estimated nitrate lifetime in this work seems high (7.69 days with ss + d) compared to the lifetime of other aerosols, particularly sulfate. Also, this work calculates a nitrate burden of 0.417 Tg N, which is around 17 times higher than those computed by *Adams et al.* [1999] (0.029 Tg N) and *Metzger et al.* [2002b] (0.024 Tg N) that did not include the contribution of sea salt and dust. The addition of this type of aerosols favors the partition of nitric acid into the particulate phase, thus enhancing aerosol nitrate formation. When sea salt and dust are neglected, the nitrate burden is reduced to 0.0152 Tg N, a value that is approximately half of other reports.

[37] The estimated lifetime of ammonium is 3.63 days, just slightly shorter of the 4.2 days reported by *Adams et al.* [1999]. The burden estimated here (0.045 Tg N with ss + d) is about 7 times smaller than that of Adams et al. (0.30 Tg N). However, if sea-salt and dust aerosol are neglected, the burden is just 12% less than Adams et al. estimate. This difference is due also to the addition of cations from sea salt and dust, which drive ammonium out of the aerosol phase. The major tropospheric sink of ammonium is wet deposition (4.32 Tg N), while dry deposition only accounts for 0.2 Tg N. Estimates by *Adams et al.* [1999] put the contribution of wet deposition at 19.5 Tg N, whereas dry deposition is set at 6.6 Tg N respectively. In contrast to

sulfate, ammonium shows a production efficiency of 0.087 which means that less than 10% of the available ammonia is converted to ammonium in the atmosphere when sea salt and dust are present.

#### 3.3. IMAGES Versus IMAGES-SCAPE2

[38] An important step toward the evaluation of potential advantages by incorporating an aerosol thermodynamic module in global models is the comparison of aerosols and gas-phase concentrations from the new coupled model with IMAGES. The following section presents a comparison between a simulation with IMAGES alone and one using the new IMAGES-SCAPE2 model. Model results are compared using the location of sites from two different monitoring networks. Stations from the Clean Air Status and Trends Network (CASTNET) are used for North America, whereas those from the Co-operative Programme for Monitoring and Evaluation of the Long Range Transmission of Air Pollutants in Europe (European Monitoring and Evaluation Programme, EMEP) are employed for Europe. Figure 7 shows the location of those sites used throughout this study from both CASTNET and EMEP.

[39] Comparison of model results between IMAGES and IMAGES-SCAPE2 is summarized in Figure 8 for aerosol species and in Figure 9 for key gas-phase precursors. In North America, sulfate concentrations calculated with IMAGES-SCAPE2 are larger than those estimated by IMAGES alone. In Europe, IMAGES-SCAPE2 predicts slightly less sulfate than IMAGES. Comparison of SO<sub>2</sub> concentrations (Figure 9) in both North America and Europe shows that both models estimate SO<sub>2</sub> in a similar manner. Differences in sulfate concentrations arise from a combination of various processes. First, sulfur emissions in the original IMAGES model differ from the ones used in IMAGES-SCAPE2. In particular, IMAGES assumes that SO<sub>2</sub> represents 97% of all sulfur emissions, whereas in the new model 100% of these emissions correspond to SO<sub>2</sub>. Second, the inclusion of dust and sea salt in IMAGES-

<sup>&</sup>lt;sup>b</sup>Chin et al. [2000a].

cKoch et al. [1999].

Table 6. Comparison of Nitrate and Ammonium Budgets With Other Studies

Budget	This	Adams	Metzger	
Component	Work <sup>a</sup>	et al. [1999]	et al. [2002a]	
Burden, Tg S				
$NO_3$	0.015 (0.417)	0.029	0.0240	
$NH_4$	0.263 (0.045)	0.300		
$NH_3$	0.071 (0.192)	0.140		
Lifetime, days				
$NO_3$	6.2 (7.69)			
$NH_4$	3.6 (3.63)	4.20		
$NH_3$	0.5 (1.35)	0.93		
Sources, Tg S/yr				
NO <sub>3</sub> production	0.89 (19.80)			
NH <sub>4</sub> production	26.97 (4.52)	26.1		
NH <sub>3</sub> emission	52.08 (52.08)	53.6		
Deposition, Tg S/yr				
NO <sub>3</sub> dry deposition	0.17 (1.11)			
NO <sub>3</sub> wet deposition	0.72 (18.69)			
NH <sub>4</sub> dry deposition	7.69 (0.20)	6.6		
NH <sub>4</sub> wet deposition	19.28 (4.32)	19.5		
NH <sub>3</sub> dry deposition	21.16 (29.35)	19.0		
NH <sub>3</sub> wet deposition	3.26 (16.70)	7.4		

<sup>a</sup>Values in parentheses include the contribution of sea-salt and dust aerosol.

SCAPE2 contributes additional sulfate emissions than the sulfur inventory used in IMAGES alone. Third, the treatment of aqueous-phase chemistry is different in both models. Specifically, S(IV) conversion to S(VI) in IMAGES-SCAPE2 now accounts for explicit dependence on H<sub>2</sub>O<sub>2</sub> and O<sub>3</sub> mixing ratios. Finally, aerosol dry and wet deposition are treated in a different manner in the coupled model. Namely, parameterizations are changed to reflect a size-resolved aerosol and to include gravitational settling.

[40] Ammonium concentrations calculated by both models are approximately equal in North America. However, Figures 8 and 9 indicate that ammonia in Europe is less likely to partition into the aerosol phase to form ammonium with IMAGES-SCAPE2. IMAGES-SCAPE2 predicts smaller ammonium concentrations over Europe than

IMAGES because ammonia partitions into the aerosol phase primarily to neutralize either nitric acid or sulfuric acid [Metzger, 2000]. Since the effect of alkaline ions from dust and sea-salt origin over Europe is considerable, the partitioning of ammonia is less favorable, thus decreasing ammonium concentrations estimated by IMAGES-SCAPE2. The decrease in ammonium is not shown by IMAGES because this model neglects any dust and sea-salt aerosol contributions. Nonetheless, the largest differences between IMAGES and IMAGES-SCAPE2 lie in the calculated nitrate and nitric acid concentrations. IMAGES-SCAPE2 predicts that nitrate concentrations are as much as 3 orders of magnitude larger than those estimated by IMAGES alone. The difference is reflected also in nitric acid, namely the concentrations predicted by IMAGES-SCAPE2 are smaller than those calculated by IMAGES. Nitrate is the aerosol species that shows the largest difference between IMAGES and IMAGES-SCAPE2, thus a further comparison between modeled values with available observations is presented in Figure 10. This figure shows that IMAGES alone underpredicts nitrate concentrations by as much as 3 orders of magnitude in both CASTNET and EMEP sites. Although IMAGES-SCAPE2 overpredicts nitrate, most modeled values still fall within a factor of 2 from observations.

#### 3.4. Modeled Versus Observed Data

[41] Evaluation of model performance by comparing predicted values with existing data at different ground-based stations is a challenging task given the model spatial resolution and the timescales involved. A thorough validation of the current model is beyond the scope of this study and can serve as the basis for a complete investigation on itself [Chin et al., 2000b]. Despite these limitations, comparisons of simulated total aerosol mass concentrations for sulfate, nitrate and ammonium with measurements from two different available databases are presented in this section. Aerosol observations made from 1987 to 1999 at 70 monitoring stations across North America are available

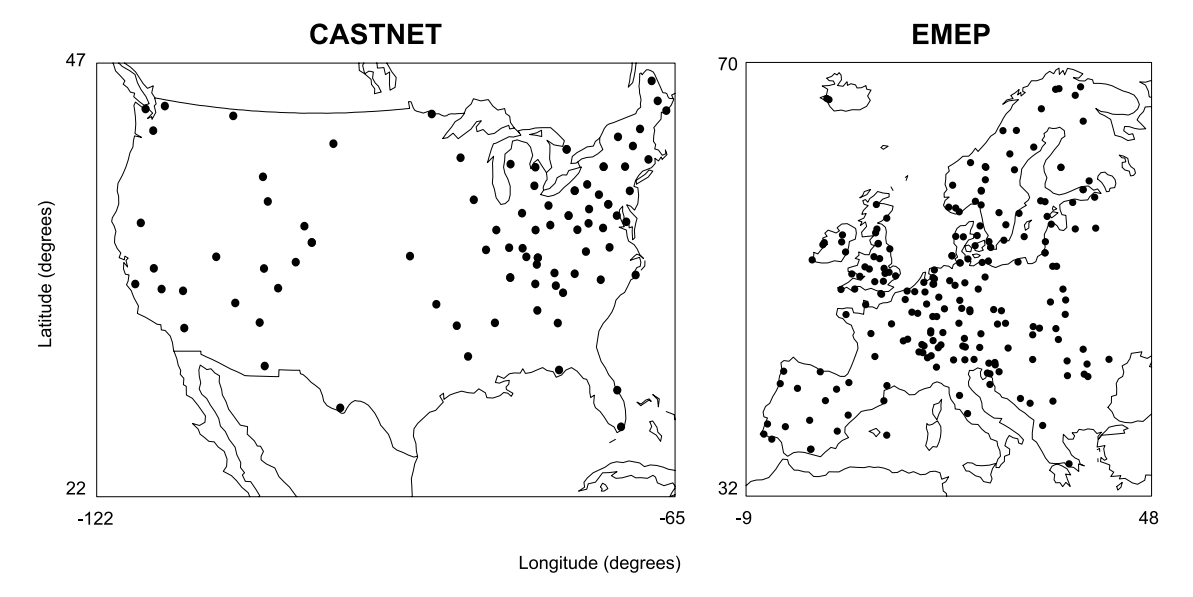


**Figure 7.** Locations of the North American sites in the CASTNET network and European sites in the EMEP network.

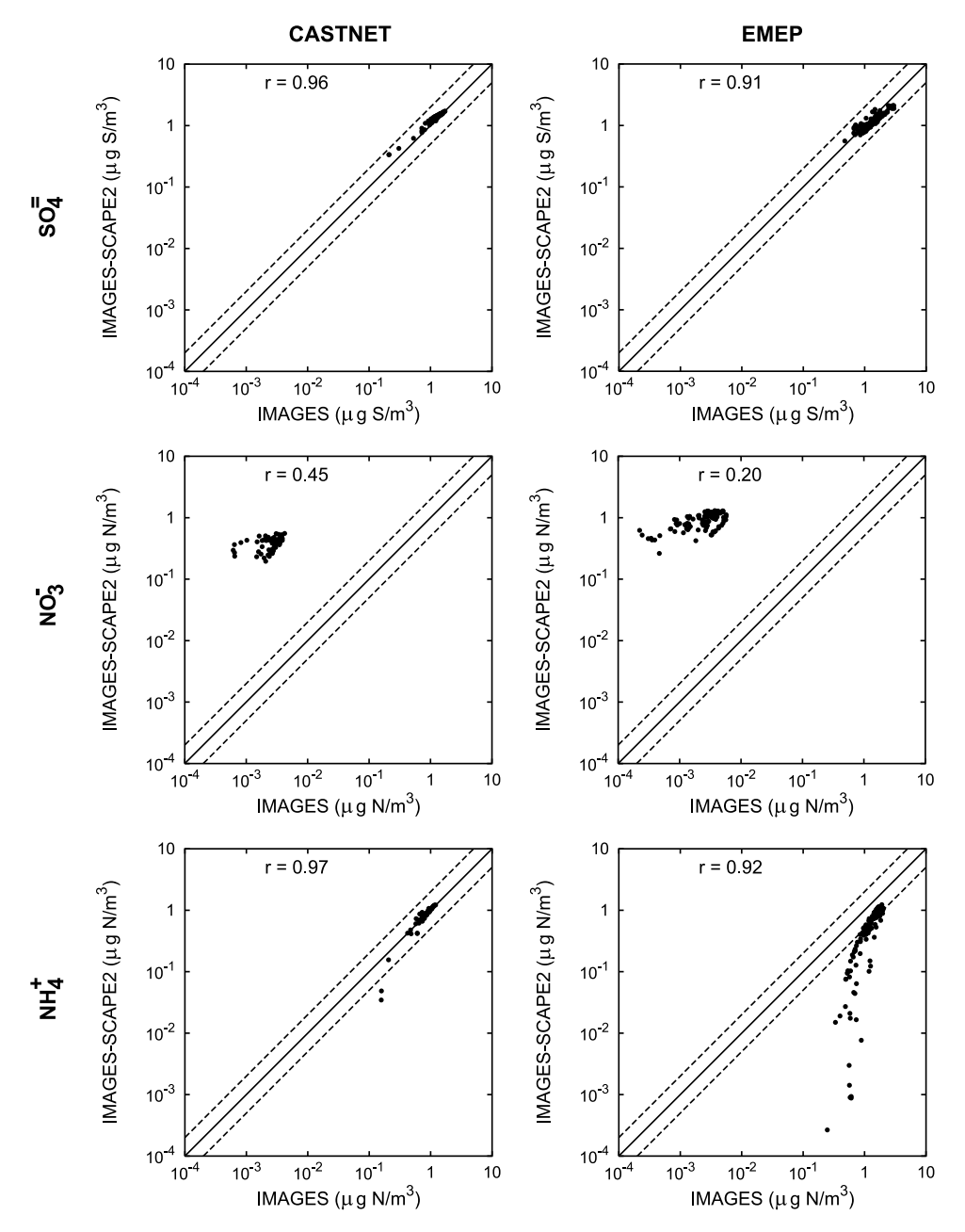


**Figure 8.** Comparison between IMAGES and coupled IMAGES-SCAPE2 modeled annual average aerosol concentrations in North American (CASTNET) and European (EMEP) sites. From top to bottom, comparisons are shown for sulfate, nitrate, and ammonium. Dashed lines indicate 2:1 and 1:2 ratios. Correlation coefficients are indicated in each plot.

from CASTNET. In addition, a comparable data set that corresponds to European measurements was obtained from (EMEP) [Hjellbrekke, 2000]. EMEP reported measurements are obtained from annual averages that span from 1978 to 2000. Data for sulfate are available from up to 123 stations. Unfortunately, not all of these sites provide as many observations for nitrate and ammonium. Measurements from all observational sites are characteristic of the aerosol load trends in highly industrialized regions where anthropogenic contributions are anticipated to be of major importance. Model results represent atmospheric concentrations of species during a typical year of the 1980 decade. Therefore arithmetic means from CASTNET and EMEP

databases are used for comparison with model outputs instead of data from any specific year. For sulfate, there are complete data to average over the entire decade. For nitrate and ammonium, however, only recent (1990s) observations are available.

[42] Figure 11 exhibits the comparisons between simulated and available observed concentration values for nitrate, ammonium, and sulfate. It is expected that the current model produces results that represent climatological trends. Thus long-term observations are better suitable for direct comparison and evaluation with this model. In order to assess whether the model underpredicts or overpredicts annually averaged concentrations, a parameter has

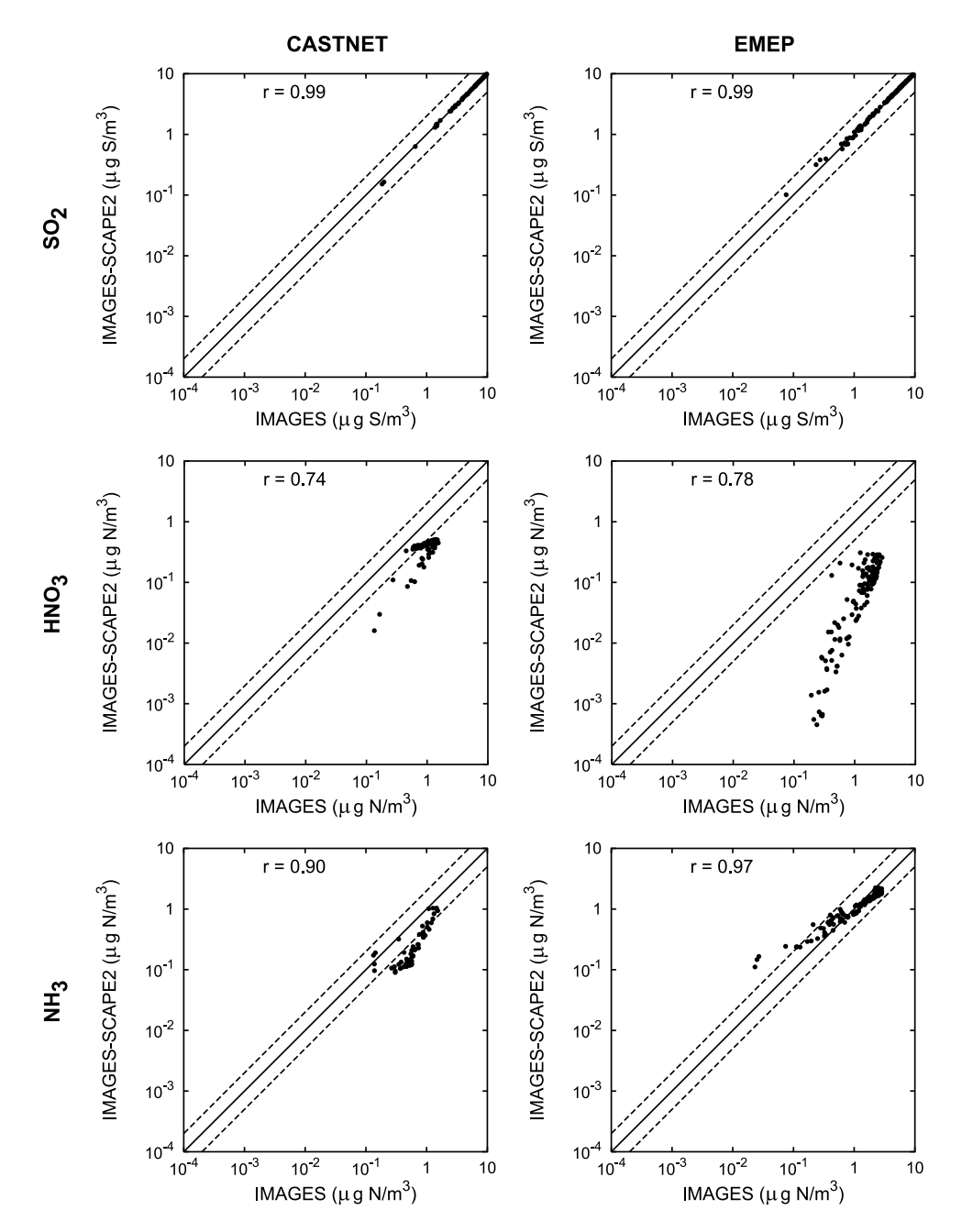


**Figure 9.** Comparison between IMAGES and coupled IMAGES-SCAPE2 modeled annual average gas concentrations in North American (CASTNET) and European (EMEP) sites. From top to bottom, comparisons are shown for sulfur dioxide, nitric acid, and ammonia. Dashed lines indicate 2:1 and 1:2 ratios. Correlation coefficients are indicated in each plot.

been defined as the slope m from a linear regression y = mx, that fits the best possible agreement between measured x and simulated y values. In addition to this parameter, correlation coefficients are calculated and indicated on each plot.

[43] For sulfate, 95% of the predicted annually averaged values fall within a factor of 2 when compared to measured data at CASTNET (72% at EMEP). Overall, data dispersion is larger over sites of the European database. The present model shows a small sulfate overprediction in North America when compared to CASTNET (slope of 1.25). In contrast, the results using EMEP show sulfate underprediction in Europe (slope of 0.51).

[44] Further analysis to compare the behavior of the model in these two regions requires SO<sub>2</sub> observational data, which is presented in Figure 12. This comparison shows that the model tends to overpredict sulfur dioxide in polluted regions of North America. Modeled SO<sub>2</sub> concentrations are a factor of 2.22 for the CASTNET sites. However in Europe SO<sub>2</sub> concentrations are slightly underpredicted (slope of 0.7). The sulfur cycle study by *Chin et al.* [2000a, 2000b] showed a similar model behavior to that exposed here. *Chin et al.* [2000b] attributed the agreement of sulfate with observed data, despite SO<sub>2</sub> overprediction, to the way sulfate is generated in polluted regions. Namely, sulfate production is controlled by H<sub>2</sub>O<sub>2</sub> concentrations

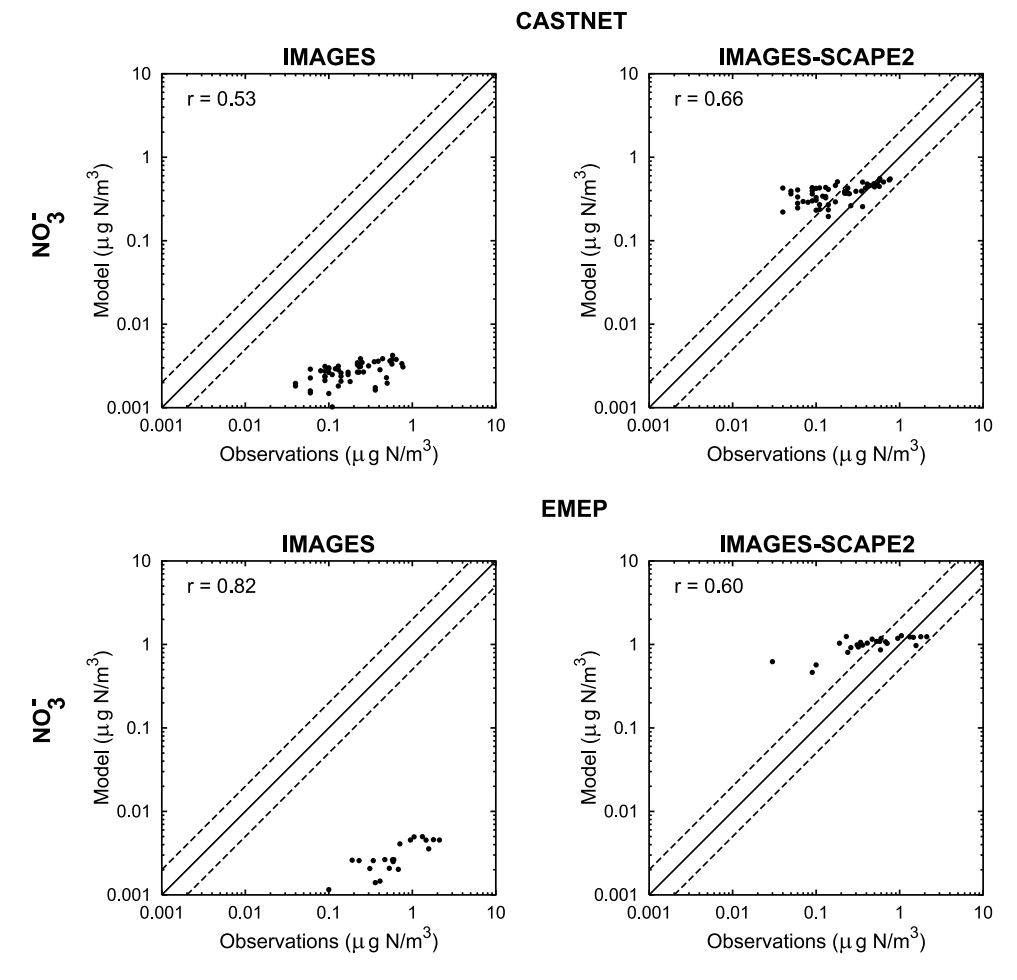


**Figure 10.** Calculated versus observed annual average nitrate concentrations in North American (CASTNET) and European (EMEP) databases. Comparison with observations is shown for both IMAGES and the new coupled IMAGES-SCAPE2 model. Dashed lines indicate 2:1 and 1:2 ratios. Correlation coefficients are indicated in each plot.

instead of  $SO_2$ . This overestimation of  $SO_2$  and the good agreement exhibited by sulfate suggest that either the  $SO_2$  emission rates used in the model are too high, or that there is a missing or underestimated sink of  $SO_2$ . Since the databases used in this work are similar to those used by *Chin et al.* [2000a], the alternative explanation to these discrepancies could also be applied to the current work. Briefly, the samples used at the sites are close to the surface (below the shallow inversion layer) and are not resolved in the model, while most  $SO_2$  is released from smoke stacks above the local inversions.

[45] Figure 11 shows that less than 60% of the simulated nitrate values fall within a factor of 2 when compared to measured data at CASTNET (50% at EMEP). Given the importance of ammonia and nitric acid as gas-phase precursors that partition into ammonium and nitrate aerosol, Figure 12 presents a comparison of simulated values of nitric acid with available observational data. Figure 12 suggests that nitric acid in the present model is in good agreement with measured data. The comparison over Europe is more difficult to assess given the insufficient amount of observational data in the region. *Müller and Brasseur* [1995] found in the original version of IMAGES, that simulated nitric acid concentrations were also in good

agreement with observations over North America. The volatile nature of nitrate makes difficult for the model to agree with measured data. Despite this mixed picture, aerosol nitrate concentrations estimated in the present study are in better agreement with measurements than the previous version of the IMAGES model. Comparison of simulated versus observed ammonium concentrations shows that 93% of the values fall within a factor of 2 at CASTNET sites, but in Europe is just less than 45%. This large discrepancy is due to the presence of a large number of cations that drive ammonium out of the aerosol phase.

[46] A North American to European nitrate concentration ratio was estimated for nitrate observations and the predictions of IMAGES and IMAGES-SCAPE2. This ratio indicates that IMAGES without sea salt and dust predicts comparable nitrate levels in both North America and Europe. However, observations show that on average European nitrate concentrations are 3 times higher than in North America (ratio of  $\approx 0.349$ ). The inclusion of sea salt and dust in the new coupled model correctly estimates this observed ratio ( $\approx 0.371$ ). Nevertheless, as elucidated above, sulfate model results are found to overpredict observations in North America and underpredict them in Europe. The most significant source of sulfate is  $SO_2$  emissions. The

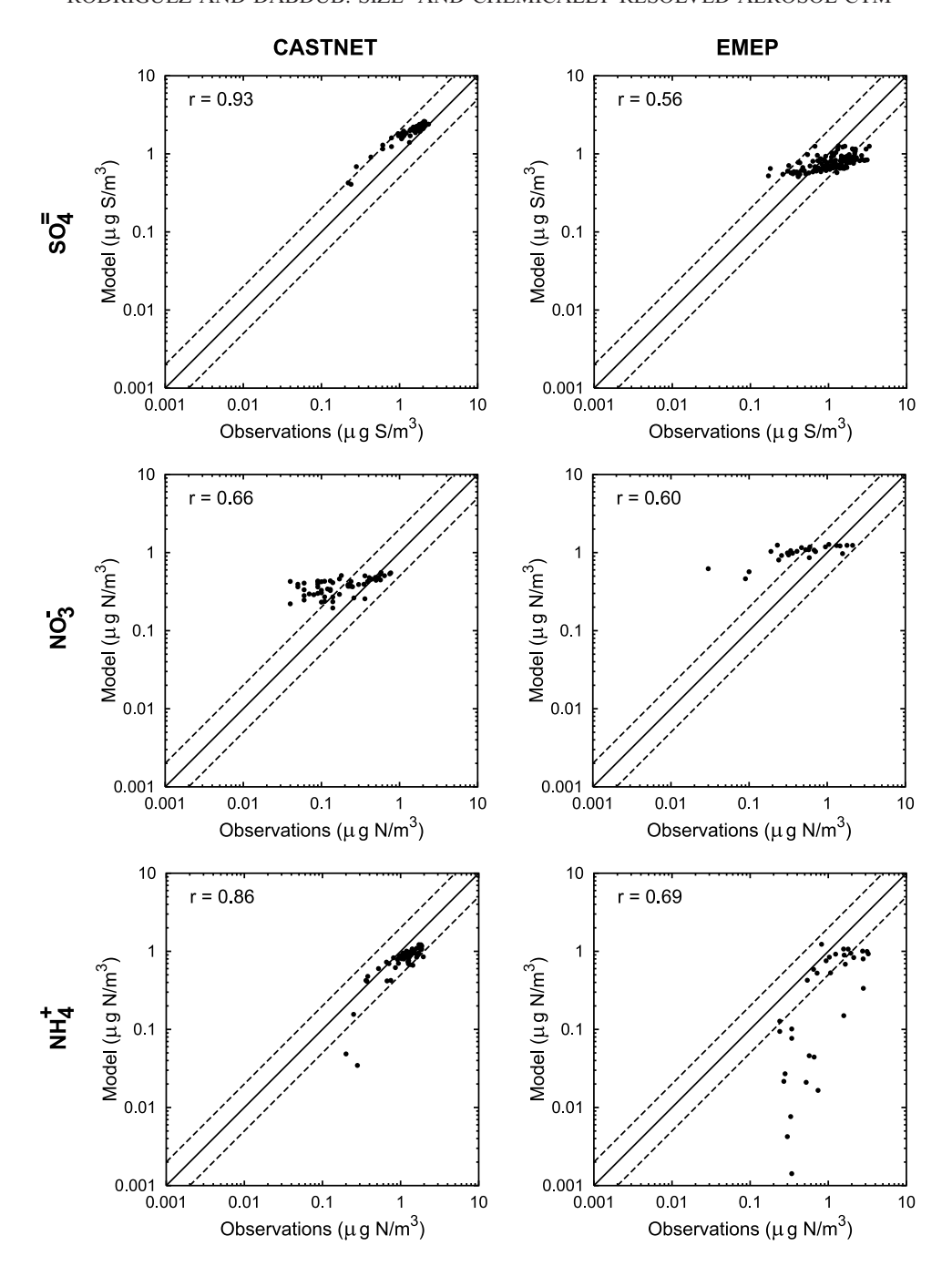


**Figure 11.** IMAGES-SCAPE2 calculated versus observed annual average aerosol concentrations in North American (CASTNET) and European (EMEP) databases. From top to bottom, comparisons are shown for sulfate, nitrate and ammonium. Dashed lines indicate 2:1 and 1:2 ratios. Correlation coefficients are indicated in each plot.

differences in sulfate concentrations presented here are due in part to the thermodynamics and not to  $SO_2$  emissions alone. The simulations performed with IMAGES alone and IMAGES-SCAPE2 use the same emissions inventory. For instance, results in Figure 9 show that even with the same emissions, IMAGES-SCAPE2 predicts higher levels of  $SO_2$  in North America and lower levels in Europe.

# 3.5. Composition and Size-Resolved Distributions

[47] In addition to global concentrations, this investigation reports chemically resolved aerosol size distributions calculated explicitly, i.e., without any assumptions regarding the shape of the size distributions. The following section presents a thorough examination of the chemical composition of aerosol size distributions at selected regions. First, results are shown for the aerosol dry mass alone in both North America and Europe. Finally, at selected sites, changes in the size distributions are studied when water mass content is included.

[48] Figures 13 and 14 show the annual average dry mass size distributions for some of the stations located in North America and Europe. Although a subset of all sites cannot

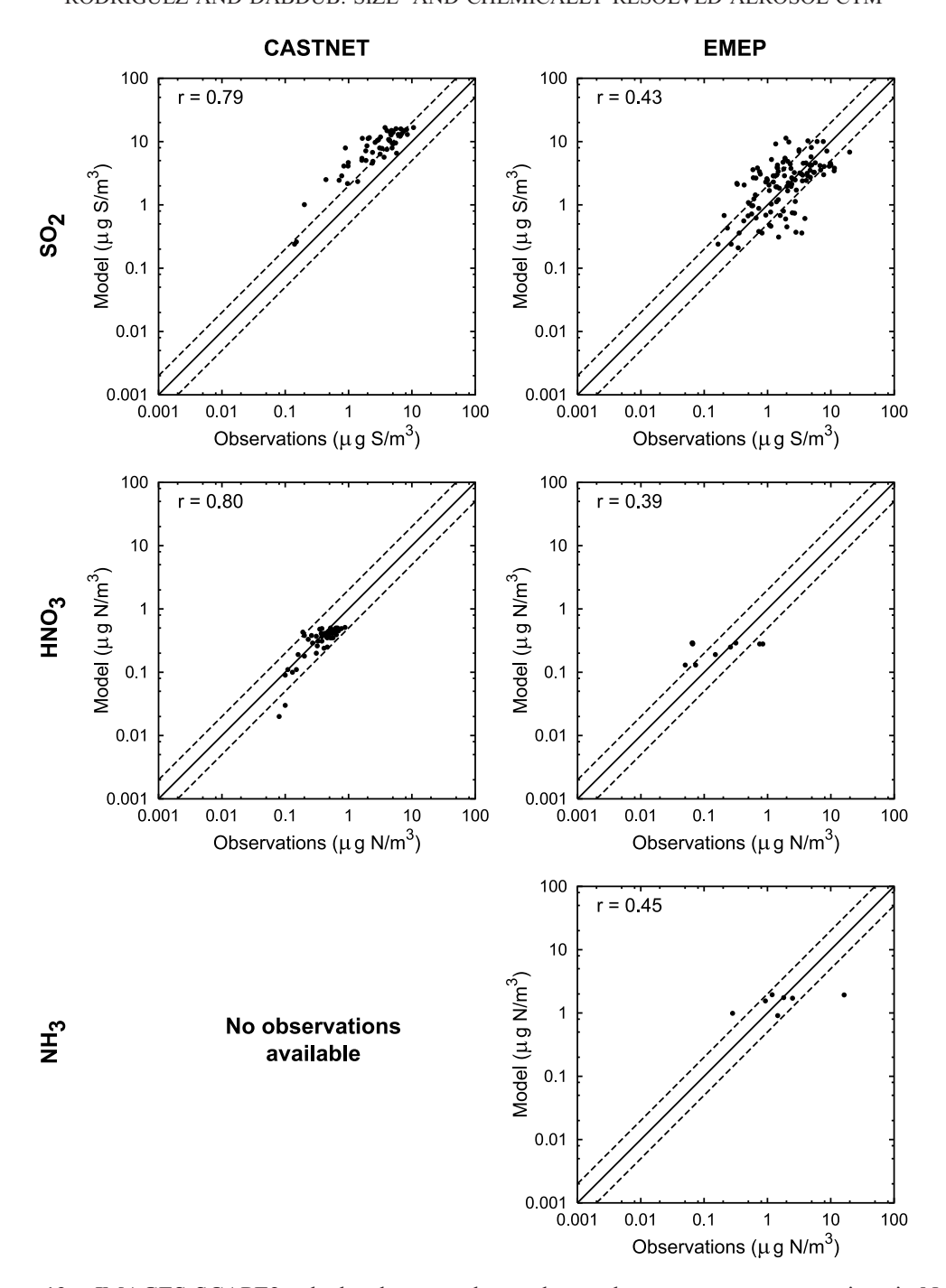


**Figure 12.** IMAGES-SCAPE2 calculated versus observed annual average gas concentrations in North American (CASTNET) and European (EMEP) databases. From top to bottom, comparisons are shown for sulfur dioxide, nitric acid, and ammonia. Dashed lines indicate 2:1 and 1:2 ratios. Correlation coefficients are indicated in each plot.

represent the full dynamics of an entire continent, results discussed here are presented as a means to illustrate the complex behavior observed in these regions. In general, model results show that the aerosol size distribution is bimodal. For typical continental polluted regions, the simulated size distributions exhibit two peaks. One of the maxima is located at approximately  $0.04-0.078~\mu m$ , while the other is located in the coarse mode between 1.25 and 2.5  $\mu m$ . This partly reflects the origin of different types of aerosol and their proximity to different sources such as

marine environments. It also reflects the potential for chemical interaction among ions. For instance, there is evidence that sea-salt aerosol displacement is a source of nitrate in the coarse mode. This displacement is anticipated to be important over coastal polluted regions. Yet, another source of coarse nitrate is nitric acid displacement reactions with calcium carbonates from dust. Modeled global mass size distributions allow the observation of the different contributions to the mass load of each size bin. An important portion of the aerosol mass loads consists of particles in

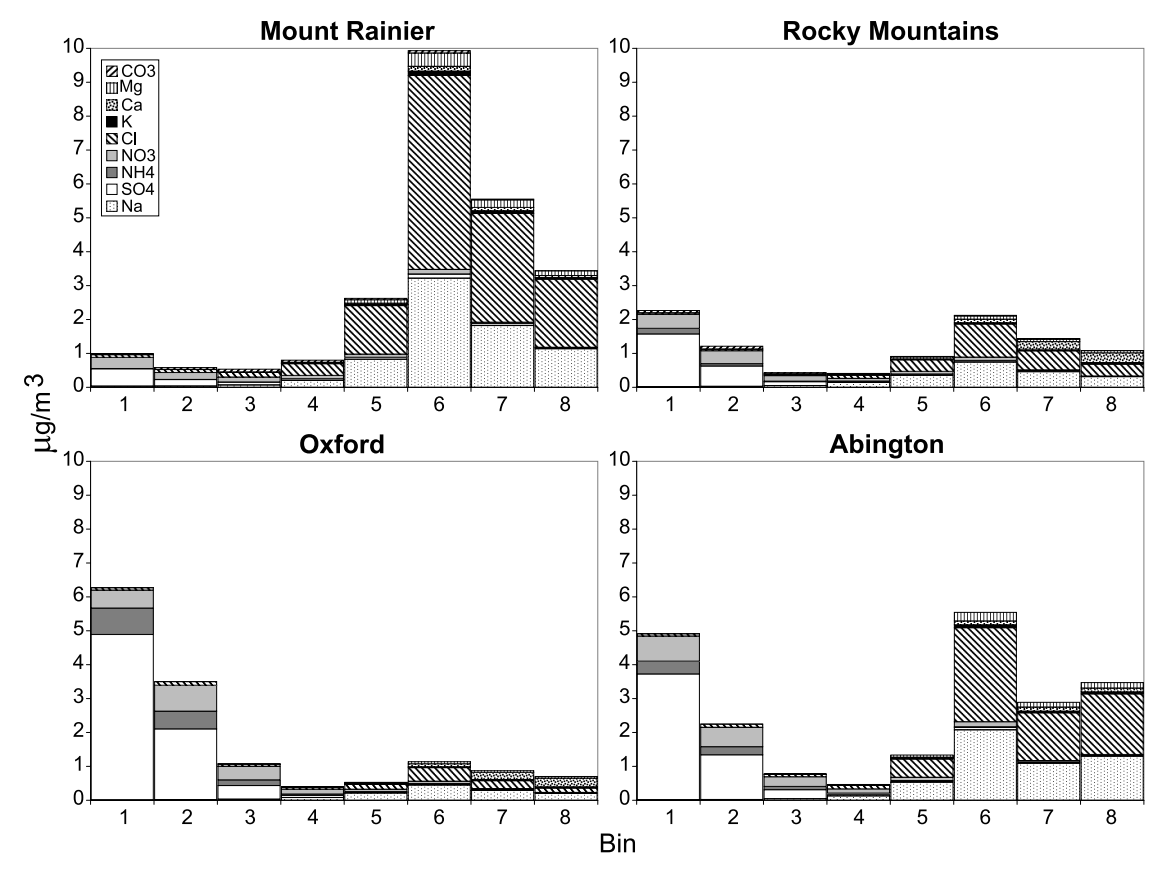


**Figure 13.** Annual average modeled size-resolved and chemically resolved dry aerosol mass size distributions at selected sites in North America (CASTNET). Diameter ranges for bins in  $\mu$ m from 1 to 8 are as follows: [0.039062, 0.078125); [0.078125, 0.15625); [0.15625, 0.3125); [0.3125, 0.625); [0.625, 1.25); [1.25, 2.5); [2.5, 5); and [5, 10].

the sub-micron range that have greater lifetimes and increased potential to undergo long-range transport.

[49] Figure 13 depicts the annual average size distribution for selected stations from the CASTNET network. Mount Rainier (46.7N, 122.1W) is located on the North American west coast. Figure 13 shows that the majority of the mass is comprised in the coarse mode, composed mostly by sodium and chlorine, revealing its coastal origin. Given the size grid in the model, this site does reflect a strong influence from the marine aerosol. When a different station is observed, for instance that over the Rocky Mountains (40.2N, 105.5W), the influence of sea-salt aerosol decreases and the importance of dust aerosol increases. This influence of sea salt on places far from the sources is attributed to the coarse resolution of the present model. A finer resolution should improve the results. Particulate nitrate, although small compared to the fraction in the fine mode, is now evident in the coarse mode. Since nitrate is never emitted directly in our model, the only mechanism that produces nitrate into the coarse mode is the chemical interaction of nitric acid with cations associated to dust. This is also apparent from the small fraction of carbonate in the fine mode, which can be interpreted as a "marker" of not aged particles [Song and Carmichael, 2001a]. We now focus our attention on the North American east coast. The eastern United States is a sulfate rich environment. The station at Oxford (39.5N, 84.7W) exemplifies the very acidic nature of this aerosol,

that when neutralized forms ammonium sulfate but that will most likely exist as bisulfate. Given the insufficient NH<sub>3</sub> levels in the eastern United States, necessary to neutralize available sulfate, nitrate is driven into the gas phase and ammonium nitrate levels are then low. These results suggest that sulfate mass distributions peak in the first bin and then get reduced across all the other bins, in contrast to ammonium and nitrate that do not seem to follow any particular distribution. Specifics on the chemical composition of the aerosol size distribution are determined in large part by the coupled aerosol module. This module uses an equilibriumbased or hybrid method that calculates at any instant, the equilibrium for volatile compounds between the gas and bulk aerosol phases and then distributes the aerosol mass increment over the size spectrum on the basis of a particle surface area weighting. Thus all aerosol species are distributed in accordance to the thermodynamical variables involved. In the case of sulfate, since is the only species that experiments nucleation, whenever this process occurs mass is placed in the first bin and this could explain its peculiar mass size distribution in our results. It is also possible that not accounted sulfate mass comes from aerosol activation to form cloud droplets, followed by subsequent evaporation to leave aerosol sulfate over the coarse mode. This kind of cloud processing is not modeled in the current study. The station at Abington (41.8N, 72.0W) is selected to observe a maritime environment on the North American

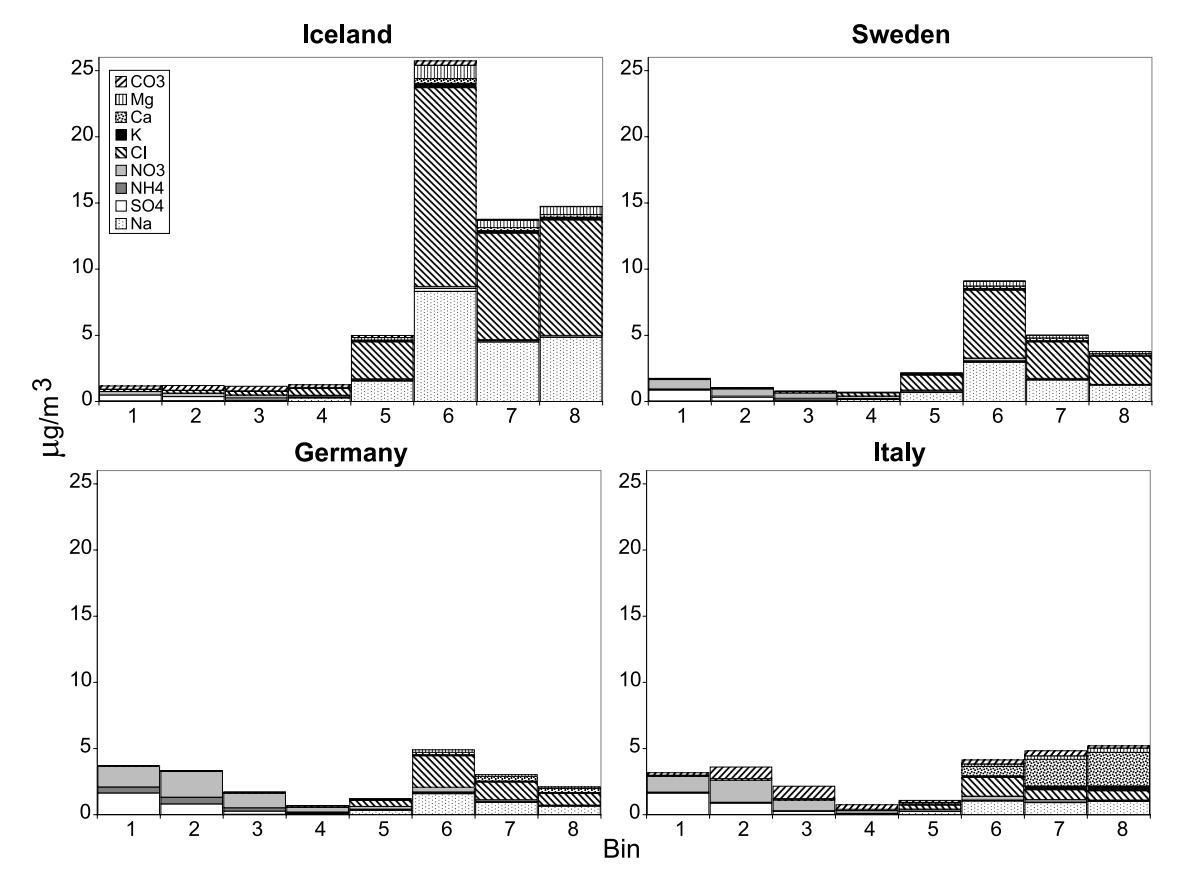


**Figure 14.** Annual average modeled size-resolved and chemically resolved dry aerosol mass size distributions at selected sites in Europe (EMEP). Diameter ranges for bins are the same as in Figure 13.

east coast. Over this site, sulfate content is high because of sulfur oxidation, but there is also a large portion of aerosol mass in the coarse mode as a result of sea-salt influence.

[50] Annual average size distributions of EMEP selected stations are shown in Figure 14. Irafoss, Iceland (64.05N, 21.01W), exhibits an aerosol distribution dominated by sea-salt. Downwind, in Bredkälen, Sweden (63.51 N, 15.20E), although there is influence by sea-salt, the formation of secondary components and their interaction with alkaline ions starts to change the overall shape and composition of the distribution. The effect of polluted sources is noticeable in places like Schmücke, Germany (50.39N, 10.46E), where a bimodal distribution is now present, with the fine mode formed mostly by nitrate, ammonium and sulfate. The southern part of Europe shows the presence of dust particles from the Sahara. For instance, Montelibretti, Italy (42.06N, 12.38E), exhibits the presence of carbonate, especially in the fine mode, which points to particles that have not been exposed to enough SO<sub>x</sub> or NO<sub>x</sub> to displace all carbonate from the aerosol. There are also considerable amounts of calcium in the coarse mode, indicative of dust aerosol reaching this region. From a chemical composition standpoint, the major difference between modeled aerosol distributions in Europe and the eastern United States is that nitrate concentrations in Europe are just as important as those of sulfate. In fact nitrate plays an important role in determining the size distributions of many European stations analyzed. Contributions from sea-salt aerosol are also important for many

stations in Europe, particularly those in the northern part of the continent. In addition, dust from Sahara sources affects the composition of aerosol by increasing the amount of alkaline ions in the coarse mode and by putting more carbonates into the fine mode. In contrast, the eastern United states is not influenced strongly by dust and most of the stations show a sulfate rich aerosol.

[51] Pilinis et al. [1995] found that direct forcing is most sensitive to changes in relative humidity and the corresponding water content of aerosols. Also, Adams et al. [2001] remarked the importance to include water uptake by aerosols in global models. The present work calculates water content of aerosol in equilibrium with the other modeled inorganic components. Figures 15 and 16 exhibit the changes in mass size distributions when water content is considered. In some of the selected sites there is the potential that water mass shifts the peaks to different size ranges than with the dry mass alone. This adjusts the general shape of the aerosol size distribution. For instance, at the station in Mount Rainier, the first peak is now shifted toward a larger diameter range. In Europe this type of phenomena is more evident. These figures emphasize the nonlinear nature of water uptake, which not only depends on ambient relative humidity and temperature, but also in the degree to which sulfate, nitrate and other anions are neutralized by ammonia, sodium and the cations associated to dust aerosol.

[52] An assumption often made is that aerosols obey a predetermined size distribution. A common approach is to

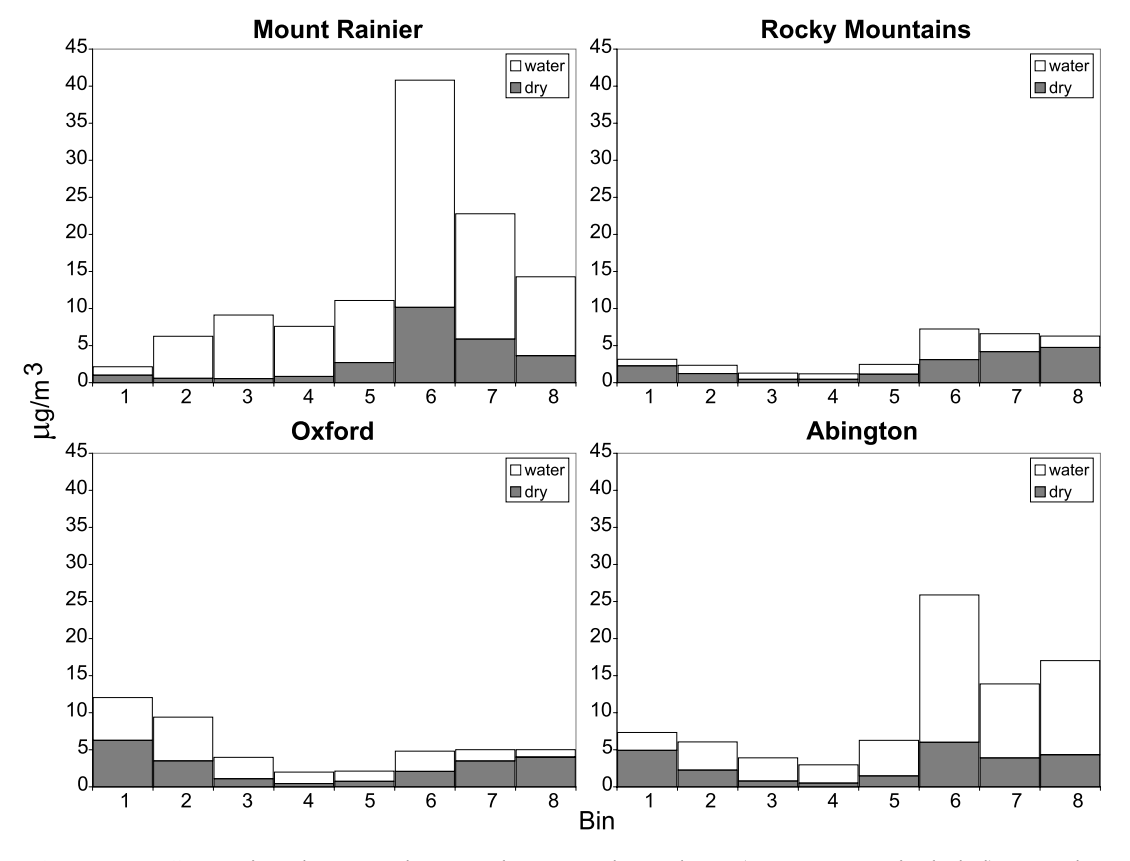


**Figure 15.** Comparison between the annual average dry and wet (water content included) aerosol mass size distributions at selected sites in North America (CASTNET). Diameter ranges for bins are the same as in Figure 13.

assume that each aerosol type follows a monomodal lognormal distribution with a prescribed mean particle radius. The combination of assumed distributions for all aerosol produces bimodal or more complex distributions. Furthermore, Dubovik et al. [2002] found that the simplest and most accurate way to simulate aerosol optical properties is by using a lognormal function. As noted above, modeled aerosols exhibit bimodal distributions. The fit of lognormal functions to model results, although possible, requires more size bins for an accurate representation. Since the present model estimates size distributions everywhere in the domain, it is possible to calculate a measure of mass diameters for each cell and then observe its variation across different geographical regions. Figure 17 shows the mean mass diameter estimated for both the fine and the coarse mode of the distributions. These estimates include not only the contribution of aerosol ions but also their water uptake. On the North American east coast, the fine mode mass mean diameter ranges from 0.1 to 0.2 µm, whereas the coarse mode diameter ranges between 2.8 and 3.6 µm. In Europe, this fine mode diameter varies from 0.2 to 0.4 µm, and the coarse mode between 2.8 and 3.6 µm. The largest particles (4.4–4.8 μm) are close to the dust sources, as shown by Figure 17b. On average, over the oceans the coarse mode diameter is relatively uniform (2.8–3.2 μm). Observational data for chemically resolved and size-resolved distribution suitable for comparison with global-scale models is scarce. However, data from the AERONET network [Dubovik et al., 1998, 2000; Dubovik and King, 2000; Smirnov et al.,

2003] of ground-based radiometers has been used to retrieve information from the aerosol mixture at different sites worldwide. Table 7 compares this work estimates of the aerosol radius in the fine and coarse modes with those values retrieved from stations reported by *Dubovik et al.* [2002]. The stations are selected to typify aerosol from the North American east coast, Europe, ocean (Lanai, Hawaii) and dust sources (Saudi Arabia). With the exception of Saudi Arabia, where dust sources are predominant, the coarse mode radius predicted by the model are consistently smaller than those retrieved from radiometers. This can be explained by the fact that the present study lacks certain type of aerosols, such as carbonaceous and organic aerosols. In contrast, the radius for estimated fine modes agrees reasonably well with observations.

### 4. Conclusions

[53] This paper presents a global modeling study that implements a detailed thermodynamical module in a three-dimensional chemical transport model in order to study the dynamics of aerosol formation. IMAGES is used as the host CTM to calculate size- and chemically resolved aerosol mass size distributions. SCAPE2 is the thermodynamical module used to calculate equilibrium concentrations among modeled aerosol species and their gas-phase precursors. Emphasis is placed in analyzing the distributions of aerosol ammonium, nitrate, and sulfate subject to interaction with sea salt and dust. All modeled species undergo transport,

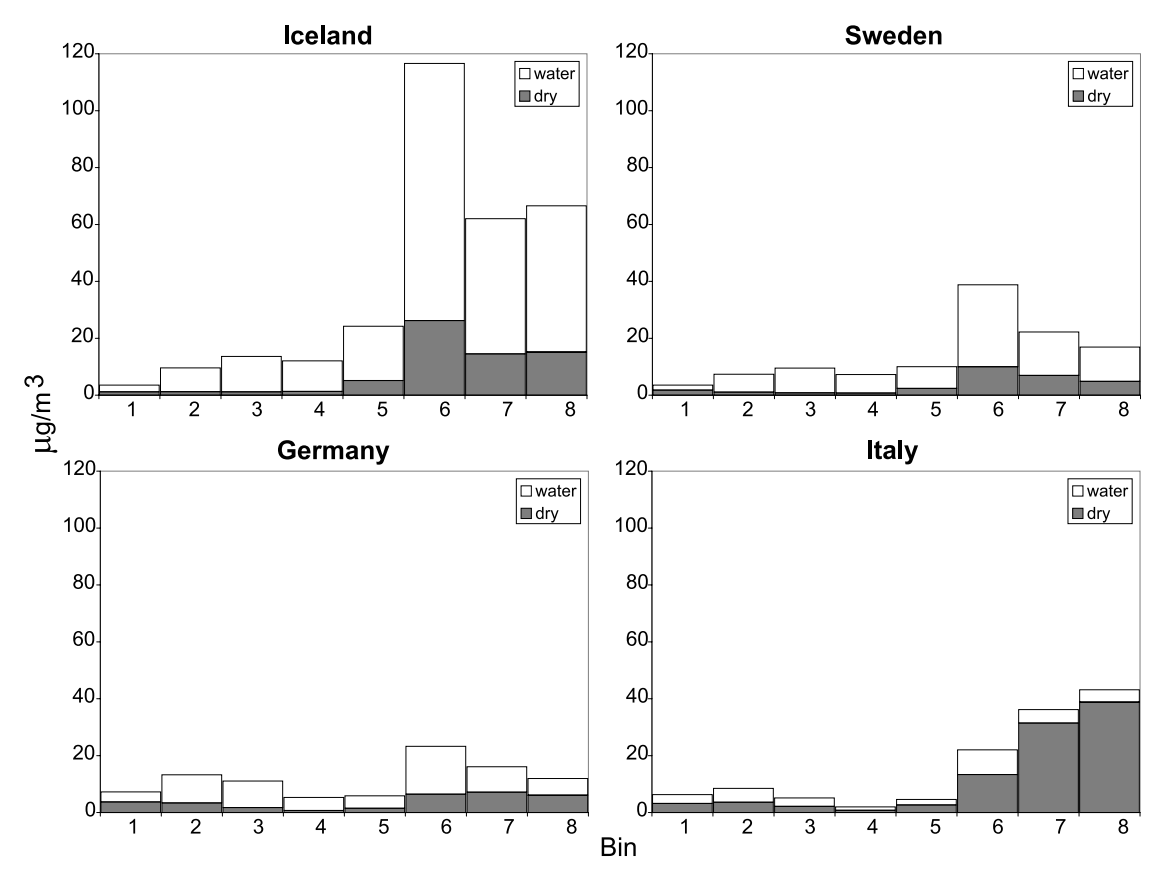


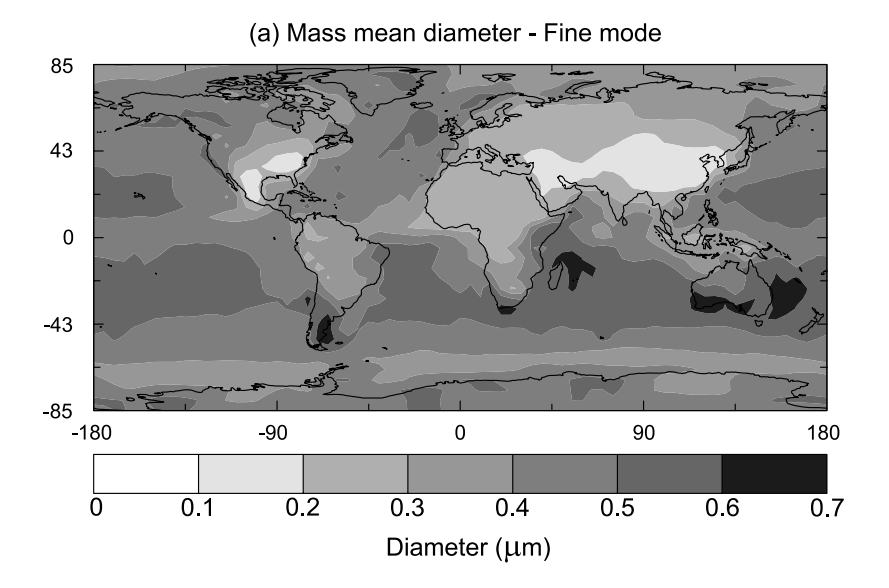
**Figure 16.** Comparison between the annual average dry and wet (water content included) aerosol mass size distributions at selected sites in Europe (EMEP). Diameter ranges for bins are the same as in Figure 13.

dry and wet deposition processes. In addition to precursor gas-phase species, the thermodynamic module requires prescribed relative humidity and temperature fields updated monthly by European Centre for Medium-Range Weather Forecasts (ECMWF) analysis. Operator splitting is used to solve the equations that represent the different physical and chemical processes modeled.

[54] This study finds that over polluted continental regions, the presence of sea-salt and dust aerosol increases 20-80% the sulfate concentration. More than 100% sulfate enhancement over the Southern Ocean is the result of including sea-salt aerosol. This enhancement is due in part to sea-salt sulfate from particulate emissions, but also to SO<sub>x</sub> displacement of carbonates from the aerosol. Estimates of annually averaged coarse mode to total sulfate ratio at surface level show that fine mode sulfate represents more than 90% of the mass in most of the continental regions. However, on the African west coast, up to 20% of the sulfate resides in the coarse mode. On average, surface nitrate concentrations are higher in Europe than on the east coast of North America. This could be the result of a decrease of sulfate in Europe (relative to North America) that is accompanied by an increase of aerosol nitrate. The highest nitrate concentrations at the surface level coincide over regions with important dust sources as Africa, Saudi Arabia and central Asia. Nitrate concentrations are lower when sea-salt aerosol are not included, particularly over nonpolluted and marine regions. Estimated nitrate enhancement varies between 14 and 60% over industrialized

regions of the world. Ammonium concentrations show a 100% decrease in surface level concentrations when compared with concentrations from a simulation with no dust and no sea-salt aerosol. The loss is not as pronounced over continental polluted regions, where the decrease ranges between 20 and 60%. Ammonium at surface level exists mostly in the fine mode. The decrease in ammonium concentrations is due to the abundance of cations from dust and sea-salt origin that inhibit NH<sub>3</sub> to partition into the aerosol phase. The lifetime of sulfate is computed to be 4.57 days. This estimate is within the range of values reported in other studies and just slightly shorter of that calculated by Pham et al. [1995]. Furthermore, the sulfate burden also falls within the range of previous estimates. Although the presence of sea salt and dust enhances the formation of sulfate at the surface level, the burden accounts for sulfate through the entire troposphere. The lifetime of nitrate is computed to be 7.69 days. This estimate is high compared with lifetimes of other aerosols, particularly sulfate. Nitrate burden is higher than Adams et al. [1999] and Metzger et al. [2002b] calculations. The difference is explained from the presence of sea-salt and dust aerosol in this study that enhances the partition of nitric acid into particulate nitrate.

[55] Comparison between simulations performed with the new model (IMAGES-SCAPE2) and IMAGES alone shows that nitrate and nitric acid are the species most influenced by introducing an aerosol thermodynamics module. Furthermore, an important finding is that nitrate is greatly under-



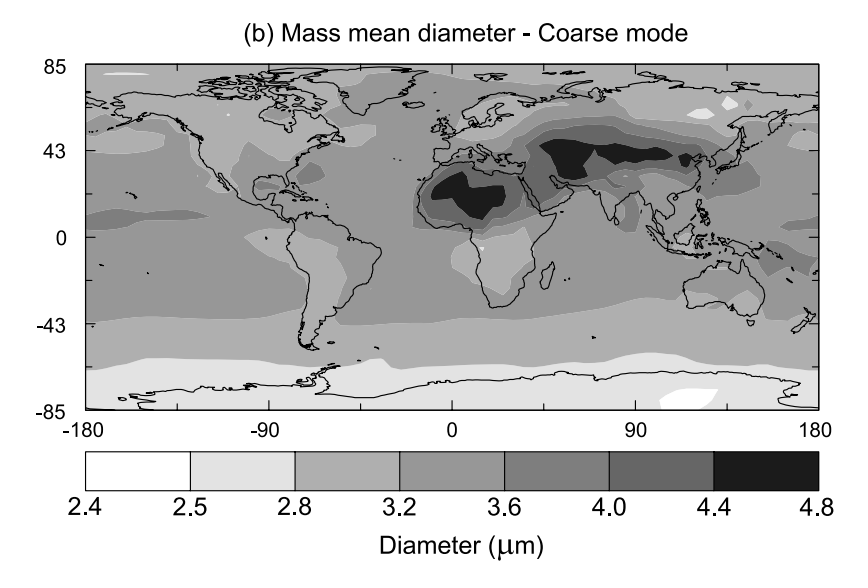


**Figure 17.** (a) Annually averaged mass mean diameter estimated with the fine mode (diameters <1.25 μm) and (b) coarse mode of the simulated aerosol size distribution. Estimates include the contribution of aerosol water content.

estimated by IMAGES alone as shown by comparison between observed and modeled concentrations. Comparison of simulated total aerosol mass concentrations with measurements from CASTNET and EMEP databases for sulfate, nitrate and ammonium show good agreement with data from the North American sites. Approximately 95% of the predicted annually averaged sulfate falls within a factor of 2 when compared to measured data at CASTNET. Overall, data dispersion is larger over sites of the European database. For nitrate, less than 60% of the simulated values fall within a factor of 2 when compared to measured data at CASTNET (50% at EMEP).

[56] Model predictions show a bimodal aerosol size distribution. This reflects both the origin of aerosol species and the chemical interaction among ions. Modeled global mass size distributions exhibit different contributions to the mass load of each bin. An important portion of the aerosol

mass load consists of particles in the sub-micron range that have greater lifetimes and an increased potential to undergo long-range transport. For example, over the east coast of North America, sulfate mass distributions tend to peak in the first bin and then decrease across all the other bins. In contrast, ammonium and nitrate do not follow any particular distribution. Sulfate is the only species that nucleates in the model, whenever this process occurs, mass is placed in the first bin. This explains the shape of the size distribution. Over polluted regions in central Europe a bimodal distribution is observed with the fine mode formed mostly by nitrate, ammonium and sulfate. The southern part of Europe shows the influence of dust particles from the Sahara. A major difference between modeled aerosol distributions in Europe and the eastern United States is the importance of nitrate concentrations in Europe. Nitrate plays an important role to determine the size distributions

**Table 7.** Comparison of Estimated Fine and Coarse Mean Mass Radius With Retrieved Values From AERONET at Selected Sites

Aerosol Mode Retrieved Radius, μm		Modeled Radius, μr		
	GSFC, Greenbelt, Maryland			
Fine	0.12	0.12		
Coarse	3.03	1.68		
	Paris, France			
Fine	0.11	0.16		
Coarse	2.76	1.60		
	Lanai, Hawaii			
Fine	0.16	0.30		
Coarse	2.70	1.77		
	Solar Village, Saudi Arabia			
Fine	0.12	0.10		
Coarse	2.32	2.16		

of many European stations. Contributions from sea-salt aerosol are also important in European stations, particularly those in the northern part of the continent. Dust from Sahara sources affects the composition of aerosol in southern Europe by increasing the amount of alkaline ions in the coarse mode and by forming carbonates into the fine mode. In contrast, the eastern United States is not influenced strongly by dust and most of the sites show an aerosol composed mainly by sulfate.

- [57] This work calculates aerosol water content aerosol in equilibrium with the other inorganic compounds. The presence of water mass shifts the maximum values of the size distribution to different size ranges, adjusting the shape of the distribution in some sites. This emphasizes the nonlinear nature of water uptake, which depends on ambient relative humidity, temperature, and the neutralization degree of the modeled ions mixture. Research indicates that using SCAPE2 produces similar mean diameters (in both fine and coarse modes) to those produced by researchers that assume lognormal functions and are also comparable to available data from radiometer retrievals. However, one of the potential advantages of using a thermodynamical module, such as SCAPE2, in global CTMs lies in the ability to implement and investigate the possible feedbacks to photolysis and the interaction of aerosols with gas-phase species.
- [58] Future work required before the model is used for other applications, such as the calculation of radiative impacts, includes the following: the implementation of a detailed wet deposition scheme, the incorporation of cloud processing and the revision of the emissions inventory to reflect any significant changes that occurred over the last decade.
- [59] Acknowledgments. This study has been supported by the Fullbright-García Robles Scholarship of the Consejo Nacional de Ciencia y Tecnología (CONACYT) and the CAREER Award grant ATM-9985025 from the National Science Foundation. Any opinions, findings, and conclusions or recommendations expressed in this material are those of the authors and do not necessarily reflect the views of the National Science Foundation. The authors are grateful to Jean-François Müller for his help in the washout description and for providing access to the IMAGES code.

# References

Adams, P. J., J. H. Seinfeld, and D. M. Koch (1999), Global concentrations of tropospheric sulfate, nitrate, and ammonium aerosol simulated in a general circulation model, *J. Geophys. Res.*, 104, 13,791–13,823.

- Adams, P. J., J. H. Seinfeld, D. M. Koch, L. Mickley, and D. Jacob (2001), General circulation model assessment of direct radiative forcing by the sulfate-nitrate-ammonium-water inorganic aerosol system, *J. Geophys.* Res., 106, 1097–1111.
- Atkinson, R., D. L. Baulch, R. A. Cox, R. F. Hampson, J. A. Kerr, and J. Troe (1989), Evaluated kinetic photochemical data for atmospheric chemistry: Supplement III, *J. Phys. Chem. Ref. Data*, 18, 881–1097.
- Barrett, E. C. (1970), Estimation of monthly rainfall from satellite data, Mon. Weather Rev., 98, 322–330.
- Benkovitz, C. M., C. M. Berkowitz, R. C. Easter, S. Nemesure, R. Wagener, and S. E. Schwartz (1994), Sulfate over the North Atlantic and adjacent continental regions: Evaluation for October and November 1986 using a three-dimensional model driven by observation-derived meteorology, *J. Geophys. Res.*, *99*, 20,725–20,756.
- Berkowitz, C. M., R. C. Easter, and B. C. Scott (1989), Theory and results from a quasi-steady-state precipitation-scavenging model, *Atmos. Environ.*, 23, 1555–1571.
- Binkowski, F. S., and U. Shankar (1995), The regional particulate matter model: 1. Model description and preliminary results, *J. Geophys. Res.*, 100, 26,191–26,209.
- Blanchard, D. C., and A. E. Woodcock (1980), The production, concentration, and vertical distribution of the sea-salt aerosol, *Ann. N. Y. Acad. Sci.*, 338, 330–347.
- Bromley, L. A. (1973), Thermodynamic properties of strong electrolytes in aqueous solutions, *AIChE J.*, 19, 313–320.
- Calvert, J. G., and S. Madronich (1987), Theoretical study of the initial products of the atmospheric oxidation of hydrocarbons, *J. Geophys. Res.*, 92, 2211–2220.
- Chin, M. A., D. J. Jacob, G. M. Gardner, M. S. Foremanfowler, P. A. Spiro, and D. L. Savoie (1996), A global three-dimensional model of tropospheric sulfate, *J. Geophys. Res.*, 101, 18,667–18,690.
- Chin, M. A., R. B. Rood, S. J. Lin, J. F. Müller, and A. M. Thompson (2000a), Atmospheric sulfur cycle simulated in the global model GOCART: Model description and global properties, *J. Geophys. Res.*, 105, 24,671–24,687.
- Chin, M. A., D. L. Savoie, B. J. Huebert, A. R. Bandy, D. C. Thornton, T. S. Bates, P. K. Quinn, E. S. Saltzman, and W. J. De Bruyn (2000b), Atmospheric sulfur cycle simulated in the global model GOCART: Comparison with field observations and regional budgets, *J. Geophys. Res.*, 105, 24,689–24,712.
- Chin, M. A., P. Ginoux, S. Kinne, O. Torres, B. N. Holben, B. N. Duncan, R. V. Martin, J. A. Logan, A. Higurashi, and T. Nakajima (2002), Tropospheric aerosol optical thickness from the GOCART model and comparisons with satellite and sun photometer measurements, *J. Atmos. Sci.*, *59*, 461–483.
- Collins, W. D., P. J. Rasch, B. E. Eaton, B. V. Khattatov, J. F. Lamarque, and C. S. Zender (2001), Simulating aerosols using a chemical transport model with assimilation of satellite aerosol retrievals: Methodology for INDOEX, J. Geophys. Res., 106, 7313–7336.
- Covert, D. S., and J. Heintzenberg (1984), Measurement of the degree of internal/external mixing hygroscopic compounds and soot in atmospheric aerosols, *Sci. Total Environ.*, 36, 347–352.
- Curry, J. A., C. D. Ardeel, and L. Tian (1990), Liquid water content and precipitation characteristics of stratiform clouds as inferred from satellite microwave measurements, J. Geophys. Res., 95, 16,659–16,671.
- Dabdub, D., L. L. DeHaan, and J. H. Seinfeld (1999), Analysis of ozone in the San Joaquin Valley of California, Atmos. Environ., 33, 2501– 2514.
- Dai, A. G. (2001), Global precipitation and thunderstorm frequencies. Part I: Seasonal and interannual variatons, *J. Clim*, *14*, 1092–1111.
- De More, W. B., S. P. Sander, R. F. Hampson, M. J. Kurylo, D. M. Golden, C. J. Howard, A. R. Ravishankara, C. E. Kolb, and M. J. Molina (1992), Chemical kinetics and photochemical data for use in stratospheric modeling: Evaluation 10, *JPL Publ.*, 92–20.
- Dentener, F. J., G. R. Carmichael, Y. Zhang, J. Lelieveld, and P. J. Crutzen (1996), Role of mineral aerosol as a reactive surface in the global troposphere, *J. Geophys. Res.*, 101, 22,869–22,889.
- Dubovik, O., and M. D. King (2000), A flexible inversion algorithm for retrieval of aerosol optical properties from Sun and sky radiance measurements, J. Geophys. Res., 105, 20,673–20,696.
- Dubovik, O., B. N. Holben, Y. J. Kaufman, M. Yamasoe, A. Smirnov, D. Tan, and I. Slutsker (1998), Single-scattering albedo of smoke retrieved from the sky radiance and solar transmittance measured from ground, *J. Geophys. Res.*, 103, 31,903–31,923.
- Dubovik, O., A. Smirnov, B. N. Holben, M. D. King, Y. J. Kaufman, T. F. Eck, and I. Slutsker (2000), Accuracy assessments of aerosol optical properties retrieved from Aerosol Robotic Network (AERONET) Sun and sky radiance measurements, J. Geophys. Res., 105, 9791–9806.
  Dubovik, O., B. N. Holben, T. F. Eck, A. Smirnov, Y. J. Kaufman, M. D.
- Dubovik, O., B. N. Holben, T. F. Eck, A. Smirnov, Y. J. Kaufman, M. D. King, D. Tanre, and I. Slutsker (2002), Variability of absorption and

- optical properties of key aerosol types observed in worldwide locations, *J. Atmos. Sci.*, 59, 590-608.
- Erickson, D. J., C. Seuzaret, W. C. Keene, and S. L. Gong (1999), A general circulation model based calculation of HCl an ClNO<sub>2</sub> production from sea-salt dechlorination: Reactive Chlorine Emissions Inventory, *J. Geophys. Res.*, 104, 8347–8372.
- Feichter, J., E. Kjellstrom, H. Rodhe, F. Dentener, J. Lelieveld, and G.-J. Roelofs (1996), Simulation of the tropospheric sulfur cycle in a global climate model, *Atmos. Environ.*, 20, 1693–1707.
- Feigelson, E. M. (1984), Radiation in a Cloudy Atmosphere, Atmos. Oceanogr. Sci. Libr., vol. 6, D. Reidel, Norwell, Mass.
  Franceschini, M., G. Pitari, and G. Visconti (1991), A study of the global
- Franceschini, M., G. Pitari, and G. Visconti (1991), A study of the global distribution of sulfate aerosols with a 2D model including microphysics, Nuovo Cimento Soc. Ital. Fis. C: Geophys. Space Phys., 14, 401– 416
- Fritsch, J. M., and C. F. Chappel (1980), Numerical prediction of convectively driven mesoscale systems: 1. Convective parameterization, *J. Atmos. Sci.*, *37*, 1722–1733.
- Fritsch, J. M., R. J. Kane, and C. R. Chelius (1986), The contribution of mesoscale convective weather systems to the warm-season precipitation in the United States, *J. Clim. Appl. Meteorol.*, 25, 1333–1345.
- Galy-Lacaux, C., G. R. Carmichael, C. H. Song, J. P. Lacaux, H. Al Ourabi, and A. I. Modi (2001), Heterogeneous processes involving nitrogeneous compounds and Saharan dust inferred from measurements and model calculations, *J. Geophys. Res.*, 106, 12,559–12,578.
- Genthon, C. (1992), Simulations of desert dust and sea-salt aerosols in Antarctica with a general circulation model of the atmosphere, *Tellus*, *Ser. B*, 44, 371–389.
- Ghan, S. J., R. C. Easter, E. G. Chapman, H. Abdul-Razzak, Y. Zhang, L. R. Leung, N. S. Laulainen, R. D. Saylor, and R. A. Zaveri (2001a), A physically based estimate of radiative forcing by anthropogenic sulfate aerosol, *J. Geophys. Res.*, 106, 5279–5293.
  Ghan, S. J., N. S. Laulainen, R. C. Easter, R. Wagener, S. Nemesure, E. G.
- Ghan, S. J., N. S. Laulainen, R. C. Easter, R. Wagener, S. Nemesure, E. G. Chapman, Y. Zhang, and R. Leung (2001b), Evaluation of aerosol direct radiative forcing in MIRAGE, *J. Geophys. Res.*, 106, 5295–5316.
- Giannakopoulos, C., M. P. Chipperfield, K. S. Law, and J. A. Pyle (1999), Validation and intercomparison of wet and dry deposition schemes using <sup>210</sup>Pb in a global three-dimensional off-line chemical transport model, *J. Geophys. Res.*, *104*, 23,761–23,784.
- Gong, S. L., L. A. Barrie, and J. P. Blanchet (1997), Modeling sea-salt aerosols in the atmosphere: 1. Model development, *J. Geophys. Res.*, 102, 3805–3818.
- Heymsfield, A. J. (1993), Microphysical structures of stratiform and cirrus clouds, in *Aerosol-Cloud-Climate Interactions*, edited by P. V. Hobbs, pp. 97–121, Academic, San Diego, Calif.
- Hjellbrekke, A.-G. (2000), Status report with respect to measurements of particulate matter in EMEP, data report 1998: Part 2. Monthly and seasonal summaries, *EMEP/CCC-Rep.* 4/2000, 257 pp., Norw. Inst. for Air Res., Lillestrøm.
- Hoffmann, M. R., and J. G. Calvert (1985), Chemical transformation modules for Eulerian acid deposition models, vol. 2, The aqueous-phase chemistry, EPA/600/3-85/017, U.S. Environ. Protect. Agency, Research Triangle Park. N. C.
- Houze, R. A., Jr. (1993), Cloud Dynamics, Academic, San Diego, Calif. Jacobson, M. Z. (1997), Development and application of a new air pollution modeling system, III, Aerosol-phase simulations, Atmos. Environ., 31, 587–608.
- Jacobson, M. Z. (2001), Global direct radiative forcing due to multicomponent anthropogenic and natural aerosols, J. Geophys. Res., 106, 1551–1568.
- Kartographisches Institut Bertelsmann (1977), Neue Welt Atlas, Reises und Verkehrsverl., Berlin.
- Kim, Y. P., and J. H. Seinfeld (1995), Atmospheric gas-aerosol equilibrium: III. Thermodynamics of crustal elements Ca<sup>2+</sup>, K<sup>+</sup>, Mg<sup>2+</sup>, *Aerosol Sci. Technol.*, 22, 93–110.
- Kim, Y. P., J. H. Seinfeld, and P. Saxena (1993a), Atmospheric gas-aerosol equilibrium: I. Thermodynamic model, *Aerosol Sci. Technol*, 19, 157– 181.
- Kim, Y. P., J. H. Seinfeld, and P. Saxena (1993b), Atmospheric gas-aerosol equilibrium: II. Analysis of common approximations and activity coefficient calculation methods, *Aerosol Sci. Technol.*, 19, 182–198.
- Knipping, E. M., and D. Dabdub (2003), Impact of chlorine emissions from sea-salt aerosol on coastal urban ozone, Environ. Sci. Technol., 37, 275– 284
- Koch, D., D. Jacob, I. Tegen, D. Rind, and M. Chin (1999), Tropospheric sulfur simulation and sulfate direct radiative forcing in the Goddard Institute for Space Studies general circulation model, *J. Geophys. Res.*, 104, 23,799–23,822.
- Kusik, C. L., and H. P. Meissner (1978), Electrolyte activity coefficients in organic processing, AIChE Symp. Ser., 173, 14–20.

- Langner, J., and H. Rodhe (1991), A global three-dimensional model of the tropospheric sulfur cycle, *J. Atmos. Chem.*, 13, 225–263.
   Liousse, C., J. E. Penner, C. Chuang, J. J. Walton, H. Eddleman, and
- Liousse, C., J. E. Penner, C. Chuang, J. J. Walton, H. Eddleman, and H. Cachier (1996), A global three-dimensional model study of carbonaceous aerosols, *J. Geophys. Res.*, 101, 19,411–19,432.
- Luecken, D. J., C. M. Berkowitz, and R. C. Easter (1991), Use of a threedimensional cloud-chemistry model to study the trans-Atlantic transport of soluble sulfur species, *J. Geophys. Res.*, 96, 22,477–22,490.
- Lurmann, F. W., A. S. Wexler, S. N. Pandis, S. Musarra, N. Kumar, and J. H. Seinfeld (1997), Modeling urban and regional aerosols, II, Application to California's South Coast Air Basin, Atmos. Environ., 31, 2695–2715.
- Madronich, S., and J. G. Calvert (1989), The NCAR Master Mechanism of the gas phase chemistry: Version 2.0, NCAR Tech. Note NCAR/TN-333+STR, Natl. Cent. for Atmos. Res., Boulder, Colo.
- Madronich, S., and J. G. Calvert (1990), Permutation reactions of organic peroxy radicals in the troposphere, *J. Geophys. Res.*, *95*, 5697–5715.
- McArdle, J. V., and M. R. Hoffmann (1983), Kinetics and mechanism of the oxidation of aquated sulfur dioxide by hydrogen peroxide at low pH, *J. Phys. Chem.*, 87, 5425–5429.
- McMurry, P. H., and M. R. Stolzenburg (1989), On the sensitivity of particle size to relative humidity for Los Angeles aerosol, *Atmos. Environ.*, 40, 497–507.
- McRae, G. J., W. R. Goodin, and J. H. Seinfeld (1982), Numerical solution of the atmospheric diffusion equation for chemically reacting flows, *J. Comput. Phys.*, 45, 1–42.
- J. Comput. Phys., 45, 1–42.
  Meigs, R. (1953), World distribution of arid and semi-arid climates, in Review of Research on Arid Zone Hydrology, UNESCO Arid Zone Programs 1, pp. 203–210, U.N. Educ., Sci., and Cult. Organ., Paris.
- Meng, Z., and J. H. Seinfeld (1996), Time scales to achieve atmospheric gas-aerosol equilibrium for volatile species, *Atmos. Environ.*, 30, 2889–2900.
- Meng, Z., J. H. Seinfeld, P. Saxena, and Y. P. Kim (1995a), Atmospheric gas-aerosol equilibrium, IV, Thermodynamic of carbonates, *Aerosol Sci. Technol.*, 23, 131–154.
- Meng, Z., J. H. Seinfeld, and P. Saxena (1995b), Gas/aerosol distribution of formic and acetic acids, Aerosol Sci. Technol., 23, 561–578.
- Meng, Z., D. Dabdub, and J. H. Seinfeld (1998), Size-resolved and chemically resolved model of atmospheric aerosol dynamics, *J. Geophys. Res.*, 103, 3419–3435.
- Metzger, S. M. (2002), Gas/aerosol partitioning: A simplified method for global modeling, Ph.D thesis, 122 pp., Univ. Utrecht, Utrecht, Netherlands, Sept. 2000.
- Metzger, S., F. Dentener, S. Pandis, and J. Lelieveld (2002a), Gas/aerosol partitioning: 1. A computationally efficient model, *J. Geophys. Res.*, 107(D16), 4312, doi:10.1029/2001JD001102.
- Metzger, S., F. Dentener, M. Krol, A. Jeuken, and J. Lelieveld (2002b), Gas/aerosol partitioning: 2. Global modeling results, *J. Geophys. Res.*, 107(D16), 4313, doi:10.1029/2001JD001103.
- Millero, F. J. (1986), The pH of estuarine waters, *Limnol. Oceanogr.*, 31(4), 839–847.
- Mishra, J. K., and O. P. Sharma (2001), Cloud top temperature based precipitation intensity estimation using INSAT-1D data, *Int. J. Remote Sens.*, 22, 969–985.
- Monahan, E. C., D. E. Spiel, and K. L. Davidson (1986), A model of marine aerosol generation via whitecaps and wave disruption, in *Oceanic Whitecaps*, edited by E. C. Monahan and G. Mac Niocaill, pp. 167–174, D. Reidel, Norwell, Mass.
- Müller, J. F., and G. Brasseur (1995), IMAGES: A three-dimensional chemical transport model of the global troposphere, *J. Geophys. Res.*, 100, 16,445–16,490.
- Müller, J. F., and G. Brasseur (1999), Sources of upper tropospheric HO<sub>x</sub>: A three-dimensional study, J. Geophys. Res., 104, 1705–1715.
- Nadstazik, A., R. Marks, and M. Schulz (2000), Nitrogen species and macroelements in aerosols over the southern Baltic Sea, *Oceanologia*, 42, 411–424.
- National Research Council (NRC) (1996), Aerosol Radiative Forcing and Climatic Change, Natl. Acad. Press, Washington, D. C.
- Nguyen, K., and D. Dabdub (2002), NO<sub>x</sub> and VOC control and its effect on the formation of aerosols, *Aerosol Sci. Technol.*, *36*, 560–572.
- Pakkanen, T. A. (1996), Study of formation of coarse particle nitrate aerosol, *Atmos. Environ.*, 30, 2475–2482.
- Pandis, S. N., and J. H. Seinfeld (1989), Sensitivity analysis of a chemical mechanism for aqueous-phase atmospheric chemistry, *J. Geophys. Res.*, 94, 1105–1126.
- Pandis, S. N., A. S. Wexler, and J. H. Seinfeld (1993), Secondary organic aerosol formation and transport: 2. Predicting the ambient secondary organic aerosol-size distribution, Atmos. Environ., Part A, 27, 2403— 2416
- Penner, J. E., C. C. Chuang, and C. Liousse (1996), The contribution of carbonaceous aerosols to climate change, in *Nucleation and Atmospheric*

- Aerosols, edited by M. Kulmala and P. E. Wagner, pp. 759-769, Elsevier
- Penner, J. E., et al. (2002), A Comparison of model- and satellite-derived aerosol optical depth and reflectivity, J. Atmos. Sci., 59, 441-460.
- Phadnis, M. J., and G. R. Carmichael (2000), Numerical investigation of the influence of mineral dust on the tropospheric chemistry of east Asia, *J. Atmos. Chem.*, 36, 285–323.
- Pham, M., J. F. Müller, G. Brasseur, C. Granier, and G. Megie (1995), A three-dimensional study of the tropospheric sulfur cycle, J. Geophys. Res., 100, 26,061-26,092
- Phillips, N. A. (1957), A coordinate system having some special advantages for numerical forecasting, J. Meteorol., 14, 184-185.
- Piketh, S. J., H. J. Annegarn, and P. D. Tyson (1999), Lower tropospheric aerosol loadings over south Africa: The relative contribution of aeolian dust, industrial emissions, and biomass burning, J. Geophys. Res., 104, 1597 - 1607
- Pilinis, C., S. N. Pandis, and J. H. Seinfeld (1995), Sensitivity of direct climate forcing by atmospheric aerosols to aerosol size and composition, J. Geophys. Res., 100, 18,739-18,754.
- Pitzer, K. S., and J. J. Kim (1974), Thermodynamics of electrolytes: IV. Activity and osmotic coefficients for mixed electrolytes, J. Am. Chem. Soc., 96, 5701-5707.
- Pye, K. (1987), Aeolian Dust and Dust Deposition, Academic, San Diego, Calif.
- Rasch, P. J., W. D. Collins, and B. E. Eaton (2001), Understanding the Indian Ocean Experiment (INDOEX) aerosol distributions with an aerosol assimilation, J. Geophys. Res., 106, 7337-7355.
- Rodhe, H., and J. Grandell (1972), On the removal time of aerosol particles from the atmosphere by precipitation scavenging, Tellus, 24, 442-
- Rossow, W. B., and R. A. Schiffer (1991), ISCCP cloud data products, Bull.
- Am. Meteorol. Soc., 72, 2–20.
  Rossow, W. B., L. C. Garder, P. J. Lu, and A. W. Walker (1987), International Satellite Cloud Climatology Project (ISCCP) documentation on cloud data, Rep. WMO/TD-266, 78 pp., World Meteorol. Organ., Geneva.
- Russell, A. G., D. A. Winner, R. A. Harley, K. F. McCue, and G. R. Cass (1993), Mathematical modeling and control of the dry deposition flux of nitrogen-containing air pollutants, Environ. Sci. Technol., 27, 2772-
- Seinfeld, J. H., and S. N. Pandis (1998), Atmospheric Chemistry and Physics: From Air Pollution to Climate Change, John Wiley, New York. Shea, D. J. (1986), Climatological atlas: 1950-1979, NCAR Tech. Note NCAR/TN-269+STR, Natl. Cent. for Atmos. Res., Boulder, Colo.
- Smirnov, A., B. N. Holben, O. Dubovik, R. Frouin, T. F. Eck, and I. Slutsker (2003), Maritime component in aerosol optical models derived from Aerosol Robotic Network data, J. Geophys. Res., 108(D1), 4033, doi:10.1029/2002JD002701
- Smith, R. M., and A. E. Martell (1976), Critical Stability Constants, vol. 4, Inorganic Complexes, Plenum, New York.
- Smolarkiewicz, P. K., and P. J. Rasch (1991), Monotone advection on the sphere: An Eulerian versus semi-Lagrangian approach, J. Atmos. Sci., 48, 793 - 810.

- Song, C. H., and G. R. Carmichael (2001a), A three dimensional modeling investigation of the evolution processes of dust and sea-salt particles in east Asia, J. Geophys. Res., 106, 18,131-18,154.
- Song, C. H., and G. R. Carmichael (2001b), Gas-particle partitioning of nitric acid modulated by alkaline aerosol, J. Atmos. Chem., 40, 1-22
- Stewart, R. W., A. M. Thompson, and M. A. Owens (1990), Atmospheric residence times for soluble species: Differences in numerical and analytical model results, Atmos. Environ., Part A, 17, 2231-2235.
- Takemura, T., H. Okamoto, Y. Maruyama, A. Numaguti, A. Higurashi, and T. Nakajima (2000), Global three-dimensional simulation of aerosol optical thickness distribution of various origins, J. Geophys. Res., 105, 17,853-17,873.
- Tegen, I., and I. Fung (1995), Contribution to the mineral aerosol load from land surface modification, J. Geophys. Res., 100, 18,707-18,726
- Tegen, I., P. Hollrig, M. Chin, I. Fung, D. Jacob, and J. Penner (1997), Contribution of different aerosol species to the global aerosol extinction optical thickness: Estimates from model results, J. Geophys. Res., 103, 23.895 - 23.915.
- Thorp, J. M. (1986), Mesoscale storm and dry period parameters from hourly precipitation data, Atmos. Environ., 20, 1683-1689
- Wang, J. (1999), Dust emissions in China and their long-range transport, M.S. thesis, Univ. of Iowa, Iowa City.
- Wesely, M. L., and B. B. Hicks (1977), Some factors that affect the deposition rates of sulfur dioxide and similar gases on vegetation, J. Air Pollut.
- Control Assoc., 27, 1110–1116.
  Wexler, A. S., and J. H. Seinfeld (1990), The distribution of ammonium salts among size and composition dispersed aerosol, Atmos. Environ., Part A, 24, 1231-1246.
- Wexler, A. S., and J. H. Seinfeld (1992), Analysis of Aerosol ammonium nitrate: Departures from equilibrium during SCAQS, Atmos. Environ., Part A, 26, 579-591.
- Wexler, A. S., F. W. Lurmann, and J. H. Seinfeld (1994), Modeling urban and regional aerosols I: Model development, Atmos. Environ., 28, 531-
- Zender, C. S., H. Bian, and D. Newman (2003), Mineral Dust Entrainment and Deposition (DEAD) model: Description and 1990s dust climatology, J. Geophys. Res., 108(D14), 4416, doi:10.1029/2002JD002775.
- Zhang, Y., and G. R. Carmichael (1999), The role of mineral aerosol in tropospheric chemistry in east Asia: A model study, J. Appl. Meteorol., *38*, 353 – 366
- Zhang, Y., Y. Sunwoo, V. Kotamarthi, and G. R. Carmichael (1994), Photochemical oxidant processes in the presence of dust: An evalution of the impact of dust on particulate nitrate and ozone formation, J. Appl.
- Meteorol., 33, 813–824. Zhang, Y., C. Seigneur, J. H. Seinfeld, M. Jacobson, S. L. Clegg, and F. S. Binkowski (2000), A comparative review of inorganic aerosol thermodynamic equilibrium modules: Similarities, differences, and their likely causes, Atmos. Environ., 34, 117-137.

D. Dabdub and M. A. Rodriguez, Department of Mechanical and Aerospace Engineering, University of California, Irvine, Irvine, CA 92697-3975, USA. (ddabdub@uci.edu)

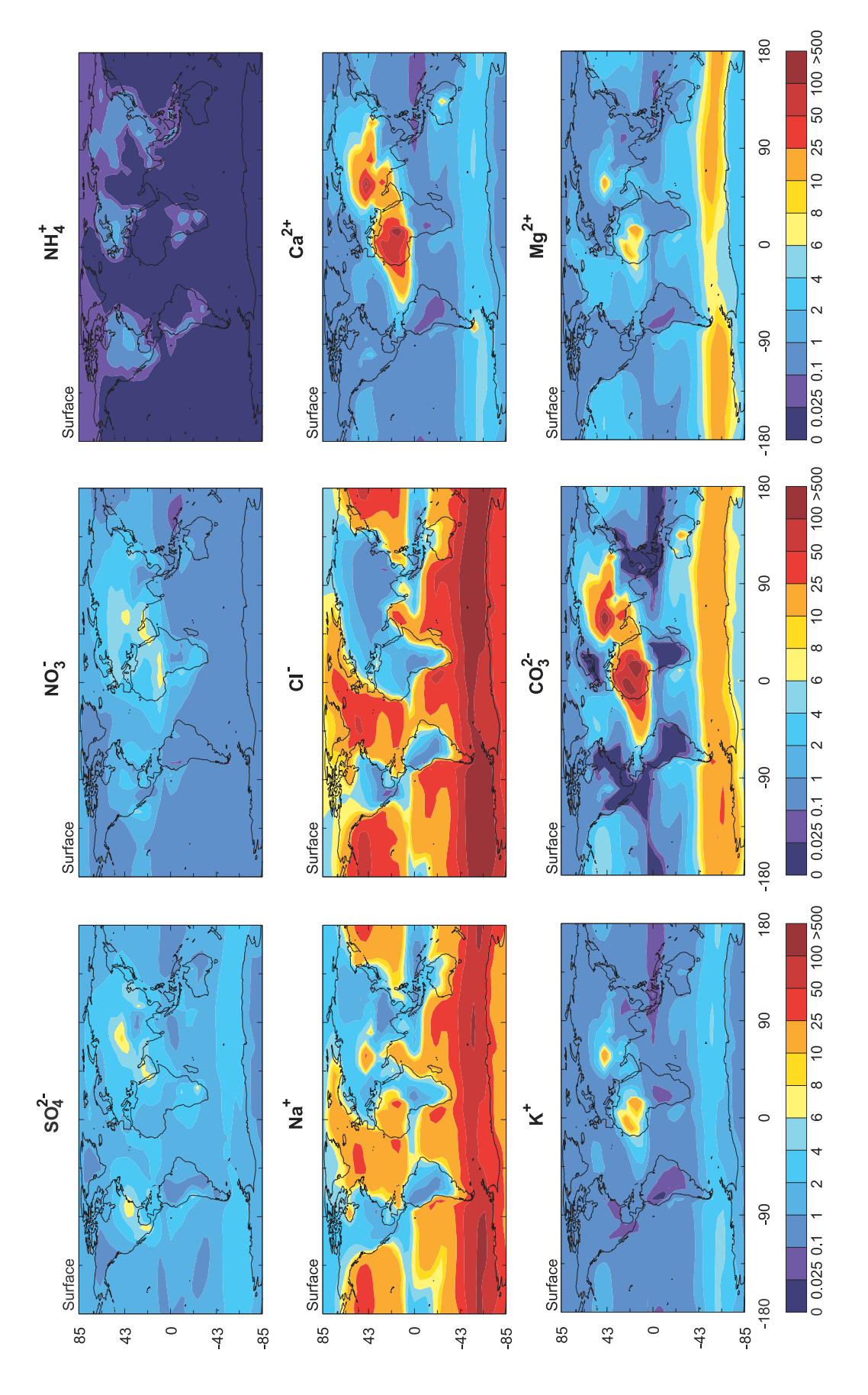


**Figure 3.** Global distributions of annual average aerosol mass concentrations calculated with IMAGES-SCAPE2 for sulfate ( $\mu g SO_4/m^3$ ), nitrate ( $\mu g NO_3/m^3$ ), ammonium ( $\mu g NH_4/m^3$ ), sodium, chloride, calcium, potassium, carbonate and magnesium ( $\mu g/m^3$ ) at surface level. All concentrations include the effect of dust and sea-salt emissions.